Article

Current Biology

Interactions between specialized gain control mechanisms in olfactory processing

Highlights

- Nonspiking compartmentalized inhibitory interneurons perform local gain control
- Inhibitory cells with broad dense arbors perform global presynaptic gain control
- Inhibitory pathways interact with each other and with short-term synaptic depression
- These interactions can reduce distortion and improve stimulus discrimination

Authors

Asa Barth-Maron, Isabel D'Alessandro, Rachel I. Wilson

Correspondence

rachel_wilson@hms.harvard.edu

In brief

Barth-Maron et al. show that different olfactory stimulus features recruit different types of inhibitory local interneurons, which perform gain control at different sites. This network architecture can minimize temporal distortions while improving odor discrimination.

Barth-Maron et al., 2023, Current Biology *33*, 1–12
December 4, 2023
https://doi.org/10.1016/j.cub.2023.10.041

CellPress

Please cite this article in press as: Barth-Maron et al., Interactions between specialized gain control mechanisms in olfactory processing, Current Biology (2023), https://doi.org/10.1016/j.cub.2023.10.041

Current Biology

CellPress
OPEN ACCESS

Article

Interactions between specialized gain control mechanisms in olfactory processing

Asa Barth-Maron,[1] Isabel D'Alessandro,[1] and Rachel I. Wilson[1,2,*]
[1]Department of Neurobiology, Harvard Medical School, 220 Longwood Avenue, Boston, MA 02115, USA
[2]Lead contact
*Correspondence: rachel_wilson@hms.harvard.edu
https://doi.org/10.1016/j.cub.2023.10.041

SUMMARY

Gain control is a process that adjusts a system's sensitivity when input levels change. Neural systems contain multiple mechanisms of gain control, but we do not understand why so many mechanisms are needed or how they interact. Here, we investigate these questions in the *Drosophila* antennal lobe, where we identify several types of inhibitory interneurons with specialized gain control functions. We find that some interneurons are nonspiking, with compartmentalized calcium signals, and they specialize in intra-glomerular gain control. Conversely, we find that other interneurons are recruited by strong and widespread network input; they specialize in global presynaptic gain control. Using computational modeling and optogenetic perturbations, we show how these mechanisms can work together to improve stimulus discrimination while also minimizing temporal distortions in network activity. Our results demonstrate how the robustness of neural network function can be increased by interactions among diverse and specialized mechanisms of gain control.

INTRODUCTION

Gain control decreases a system's gain when input is high, while allowing the gain to increase when the input is low. In general, this is achieved by an element that integrates the system's response over time and uses the integrated signal to attenuate the system's input or the system's response (Figure 1A). The intensity of natural sensory stimuli can vary over many orders of magnitude, requiring sensory systems to employ some form of gain control or adaptation to resolve features across the entire range of intensity scales.[1,2]

Interestingly, it seems that most sensory systems have multiple nested mechanisms for gain control (Figure 1B). For example, in the retina, photoreceptors implement gain control with regard to luminance, whereas local interneurons implement gain control with regard to spatial contrast. These mechanisms are specialized to control gain with regard to different stimulus features.[4] Theoretical work has demonstrated that a sensory system can transmit stimuli over a wider range of timescales when it contains multiple nested mechanisms of gain control.[5] However, we still do not fully understand how different gain control mechanisms work together within the same sensory system.

In the *Drosophila* antennal lobe, gain control is important because the relevant stimuli (odors) can vary over a vast dynamic range.[6] The key cell types in this network are olfactory receptor neurons (ORNs), projection neurons (PNs), and local neurons (LNs) (Figure 1C). There are multiple sites of gain control in this system. For example, adaptation reduces olfactory transduction in ORNs,[7] whereas short-term synaptic depression at ORN → PN synapses reduces PN responses to high ORN firing rates.[8] Additionally, LNs inhibit ORN axon terminals and PN dendrites.[9,10] These LNs are morphologically and physiologically diverse,[10–19] but it is not known how these specializations might promote effective gain control.

Recently, the detailed circuitry of the antennal lobe has been captured in several large-scale electron microscopy (EM) datasets,[20–23] four major classes of LNs (Patchy, Broad, Regional, and Sparse).[3] Notably, the majority of interneuron output synapses arise from just two of these classes, Patchy and Broad.[3] Each Patchy cell arborizes in a random handful of olfactory glomeruli, with the Patchy population collectively tiling the entire network. By contrast, each Broad LN arborizes in most or all glomeruli. Thus, both Patchy and Broad LNs are positioned to control the gain of the entire network, but we do not know why their morphologies should be so different nor whether they are specialized for distinct functions. Whatever their specializations, this diversity is likely to be fundamental to olfactory processing, given that the vertebrate olfactory bulb also contains a wide variety of inhibitory interneurons.[24–27]

In this study, we set out to investigate the functional specializations of specific Patchy and Broad cells in the *Drosophila* antennal lobe. We find that different stimulus features preferentially recruit different types of inhibitory local interneurons, which perform gain control at different sites. We show how this network architecture can minimize temporal distortions while improving odor discrimination. These results shed light on the general problem of how network output can be adaptively regulated by multiple feedback loops chained together in series.

RESULTS

Identifying LNs positioned to perform gain control

Our goal in this study was to understand the functional specializations of antennal lobe LNs. Previous functional studies[10–19]

Please cite this article in press as: Barth-Maron et al., Interactions between specialized gain control mechanisms in olfactory processing, Current Biology (2023), https://doi.org/10.1016/j.cub.2023.10.041

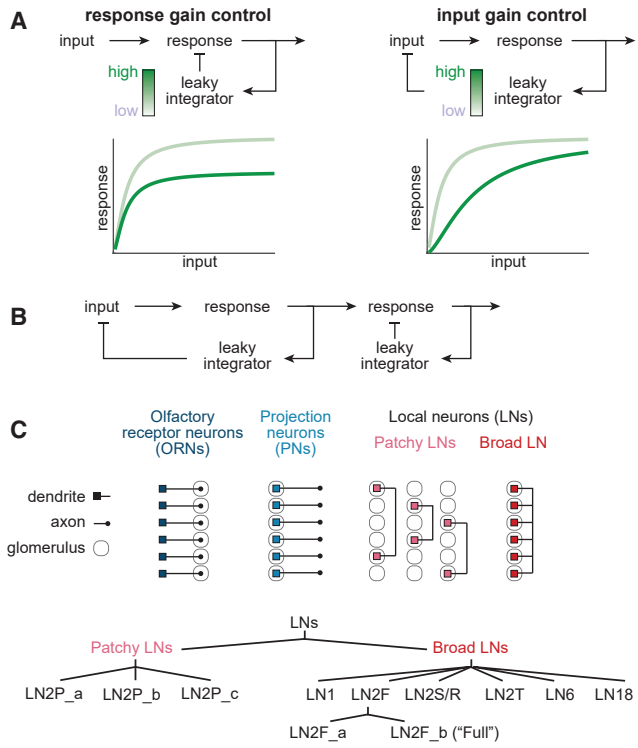

Figure 1. Multiple mechanisms of gain control

(A) Gain control (or adaptation) involves an integrator that accumulates the system's response over time. This integrated value is used to decrease the system's response or the system's input.

(B) Many sensory systems contain multiple mechanisms of gain control, which can function as negative feedback loops chained together in series.

(C) Each glomerulus in the *Drosophila* antennal lobe is targeted by a single ORN type. Postsynaptic PNs can have a dendrite in one glomerulus (uPNs) or multiple glomeruli (mPNs). Inhibitory local neurons are diverse, but most LN output synapses arise from Patchy or Broad LNs. Each Patchy cell arborizes in a handful of olfactory glomeruli, whereas each Broad LN arborizes in most glomeruli. Patchy and Broad LNs can be anatomically classified into several types.[3]

have been hindered by the lack of highly selective genetic reagents; hence, we set out to find genetic lines selective for particular LN types. We identified lines targeting LNs and used the multi-color flip-out methodology[28] to sparsely label individual cells within each candidate line of interest. By comparing individual cells with morphologies from EM connectome data,[3,20] we identified four specific Gal4 lines targeting different types of antennal lobe LNs (Figures 2A and 2B).

The first line is highly specific for Patchy cells.[15] Patchy cells comprise three subtypes—LN2P_a, LN2P_b, and LN2P_c. Each subtype completely tiles the antennal lobe, and individual cells within a subtype do not overlap. The line we identified must target one Patchy subtype because it also tiles the antennal lobe without overlap (Figure S1) We provisionally refer to this as LN2P_x and will later provide evidence that it likely targets the LN2P_c subtype. The second Gal4 line we identified targets Full cells (LN2F_b), a type of Broad LN with an unusually dense or full morphology that fills the entire antennal lobe except for glomerulus VL1. The third line targets LN1, another type of Broad LN; this cell type selectively innervates the core of each glomerulus.[14,29,30] The last line targets two types of LNs, LN2S (a Broad type named for its star-like primary branch point) and LN2R (a Regional type that resembles LN2S). We used automated image classification algorithms[31] to confirm that all these cells in the connectome are GABAergic, as expected. All of these LNs are also axonless, with pre- and post-synaptic sites intermingled throughout their dendritic arbor.[3]

Notably, connectome data indicate that Patchy and Full cells receive most of their synaptic input from ORNs and PNs (Figures 2C and S1); hence, they should be excited by odor stimuli. By contrast, LN1 and LN2S/R receive more input from LNs. In these latter cell types, we might predict that odor stimuli would drive inhibition or else balanced excitation and inhibition.

To test these predictions, we used *in vivo* patch-clamp recordings and two-photon calcium imaging to monitor LN responses to different concentrations of the same broadly activating odor (2-heptanone).[32] Like most odor stimuli, 2-heptanone recruits few ORN spikes at low concentrations but many ORN spikes at high concentrations.[6] Note that most LNs are relatively untuned to odor identity[10,13–18]; hence, we focus here on odor concentration rather than odor identity.

We found that increasing odor concentration caused modest increases in depolarization and calcium in Patchy cells (Figures 2D, 2E, and S2). Meanwhile, increasing odor concentration caused robust increases in depolarization and calcium in Full cells. By contrast, for LN1 and LN2S/R, we found that individual cells could be excited or inhibited by odor (Figures 2D, 2E, and S2), but in many cells, responses did not change much with increasing odor concentration, as we would expect if excitatory and inhibitory inputs to these cells are nearly balanced. These results support our functional predictions based on connectome data.

Together, these results imply that only a subset of LNs are positioned to perform gain control—namely, the LNs that respond to increasing odor intensity with increasing depolarization. Only these LNs would be positioned to reduce the gain of the network when odor stimuli are intense. By contrast, the LNs that are inhibited by increasing odor concentration are likely performing some other function, e.g., to suppress background noise in the network when odor stimuli are absent. These results motivated us to focus specifically on Patchy and Full cells as likely mediators of gain control. Neither of these cell types has been physiologically characterized by previous studies.

LNs specialized for intra-glomerular inhibition

Next, we focused on Patchy cells. The discrete tufts within each Patchy cell are separated by long, thin, tortuous processes (Figures 3A, S1, and S3), which should create barriers to voltage propagation and calcium diffusion. Their morphology suggests that these cells are functionally compartmentalized.

Interestingly, in our electrophysiological recordings from Patchy cells, we never observed spikes in response to either odor stimuli (Figure 3B) or direct current injection (Figure 3C). In this regard, these LNs are unusual, as most *Drosophila* antennal lobe LNs are spiking neurons.[11,12,15–19] The use of graded potentials in these cells might promote compartmentalized signaling because it would allow each tuft to operate independently.

Please cite this article in press as: Barth-Maron et al., Interactions between specialized gain control mechanisms in olfactory processing, Current Biology (2023), https://doi.org/10.1016/j.cub.2023.10.041

CellPress
OPEN ACCESS

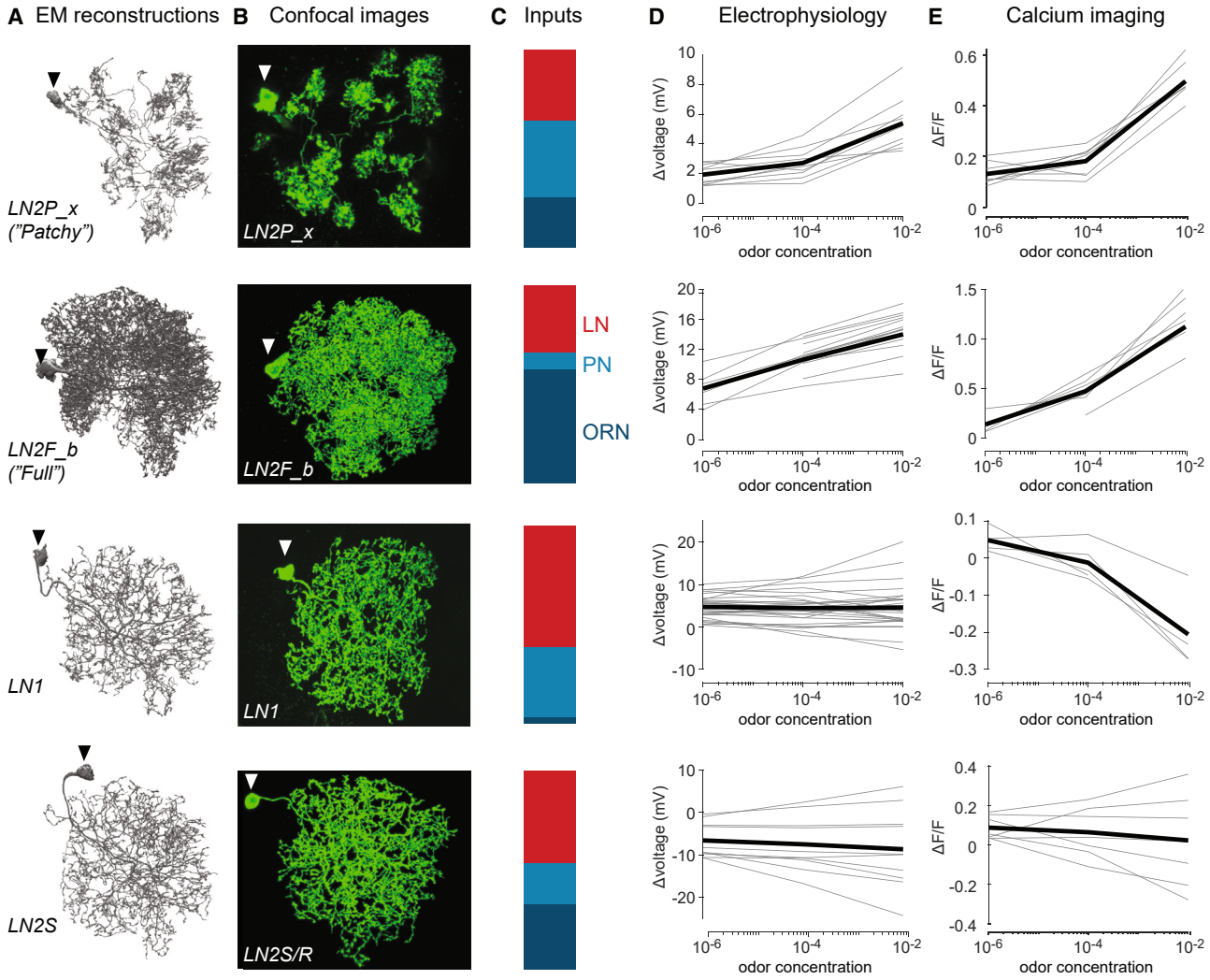

Figure 2. Identifying LNs positioned to perform gain control

(A) Four LNs reconstructed from the hemibrain EM dataset. Arrowheads point to somata. Three cells are Broad LNs, whereas one is a Patchy cell (LN2P_x). Dorsal is up; lateral is left.

(B) One example cell from each of four selective Gal4 lines (maximum z-projections of confocal stacks). Arrowheads point to somata. LN2S/R targets a mixture of LN2S and LN2R. Number of labeled cells per hemisphere (mean ± SEM) is 2.29 ± 0.19 (LN2F_b), 5 ± 0.24 (LN2P_x), 16.5 ± 0.66 (LN1, *NP1227-Gal4*), 14 ± 0.58 (LN1, *R70A09-Gal4*), and 8.56 ± 0.18 (LN2S).

(C) Fraction presynaptic inputs to each LN type arising from LNs, PNs, and ORNs. Almost all LNs are inhibitory, whereas ORNs and PNs are excitatory.

(D) Change in membrane voltage versus odor concentration (2-heptanone dilution in paraffin oil). Thin lines are individual cells, thick lines are the mean across cells. Number of cells tested for each concentration (10^{-6}, 10^{-4}, 10^{-2}): n = 10, 10, 10 (LN2P_x), n = 6, 14, 17 (LN2F_b), n = 29, 29, 29 (LN1), and n = 10, 10, 10 (LN2S/R).

(E) Normalized change in GCaMP7f fluorescence (ΔF/F) versus odor concentration (2-heptanone). Thin lines are individual cells, and thick lines are the mean across cells. Number of cells tested for each concentration (10^{-6}, 10^{-4}, 10^{-2}): n = 8, 8, 7 (LN2P_x), n = 5, 6, 8 (LN2F_b), n = 5, 5, 4 (LN1), and n = 5, 5, 5 (LN2S/R). ΔF/F is calculated over the entire antennal lobe neuropil.

See also Figures S1 and S2.

To test the idea that Patchy cells are more compartmentalized than broad LNs, we examined the spatial spread of calcium signals in these cells. Here, we selected a stimulus that is relatively selective for a single ORN type—a low concentration of farnesol, which selectively targets DC3 ORNs.[33] We observed that this "private odor" evoked robust calcium signals in Patchy cells, and these signals were largely confined to glomerulus DC3 (Figures 3D, 3E, and S3). By contrast, in Full cells, farnesol-evoked calcium signals were not so confined to DC3 (Figures 3D, 3E, and S3). Given that farnesol is relatively selective for DC3 ORNs, this result implies that there is more spatial spread of calcium signals in Full cells, compared with Patchy cells.

Next, we tested an odor stimulus that drives high firing rates in many ORN types—a high concentration of 2-heptanone. DC3 ORNs show essentially no response to even the highest

Please cite this article in press as: Barth-Maron et al., Interactions between specialized gain control mechanisms in olfactory processing, Current Biology (2023), https://doi.org/10.1016/j.cub.2023.10.041

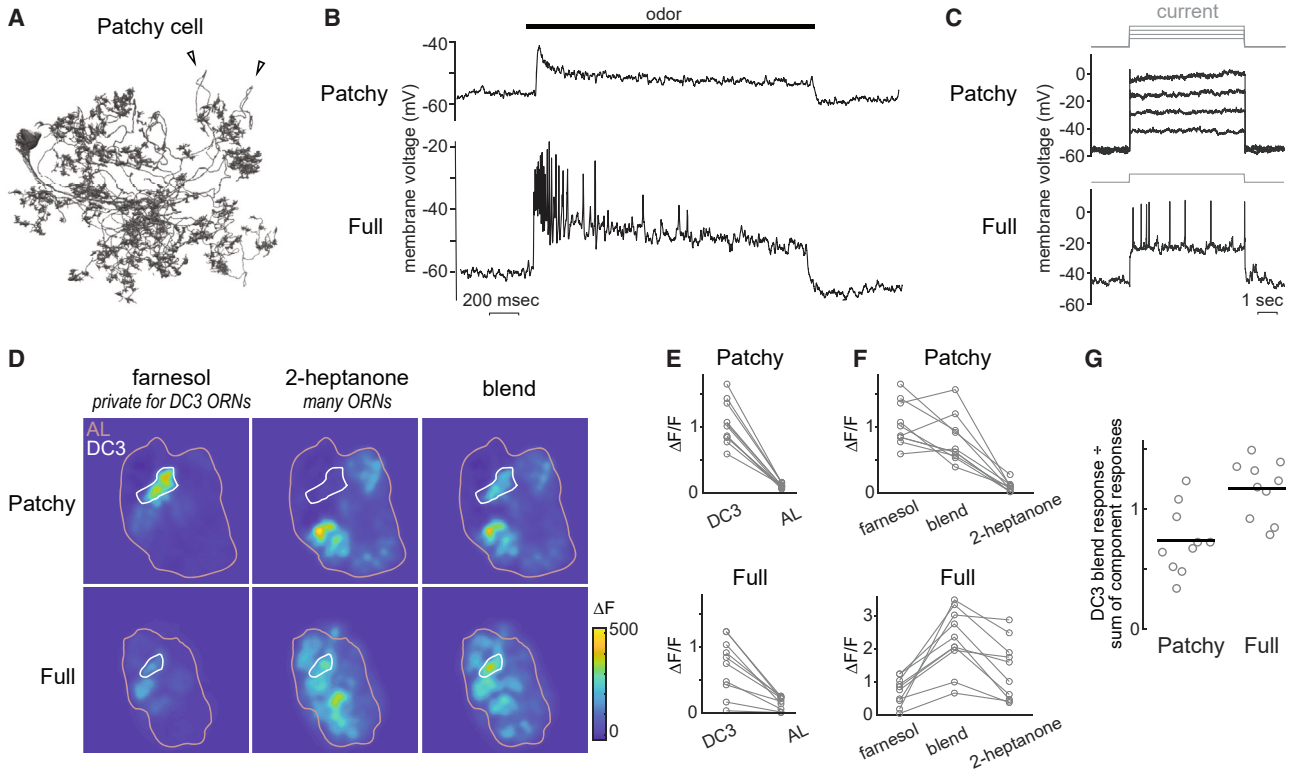

Figure 3. LNs specialized for intra-glomerular inhibition

(A) Morphology of a Patchy cell reconstructed from the hemibrain EM dataset. Arrowheads point to narrow, tortuous neurites.

(B) Example Patchy cell odor response, recorded in whole-cell current clamp mode (2-heptanone 10^{-2}, horizontal bars show timing of 2-s odor pulses). An example response from a Full cell is shown for comparison.

(C) Example Patchy cell response to depolarizing current pulses (3-s pulses of 50, 75, 100, and 125 pA). An example response from a Full cell is shown for comparison.

(D) Odor-evoked changes in fluorescence in Patchy and Full cells (shown here as ΔF rather than ΔF/F because baseline fluorescence F was very small and noisy at some regions of these images). Outlines show glomerulus DC3 and the entire antennal lobe (AL). Farnesol (10^{-4}) is a private odor for DC3 ORNs, whereas 2-heptanone (10^{-2}) drives strong activity in a broad population of ORNs. We also tested a blend of both odor stimuli.

(E) Responses to farnesol (10^{-4}) in two spatial zones, DC3 and the rest of the antennal lobe. Each set of connected points is one experiment. There is a significant interaction between cell type and spatial zone (two-way ANOVA, $p = 0.035$), indicating that Patchy cells are more highly compartmentalized.

(F) Comparing responses to all three stimuli in DC3. Each set of connected points is one experiment. In Patchy cells, the response to the blend is significantly smaller than the response to farnesol alone ($p = 0.034$, linear mixed-effects model). In Full cells, the response to the blend is significantly larger than the response to farnesol alone ($p = 5.29 \times 10^{-8}$, linear mixed-effects model).

(G) Blend response ÷ sum of the component responses, in DC3. Symbols are single experiments, lines are means. This ratio is significantly smaller for Patchy cells than for Full cells ($p = 6.04 \times 10^{-6}$, two-sample t test).

See also Figure S3.

concentrations of 2-heptanone,[33] and we found that DC3 PNs had similarly small responses to this odor (Figure 6). We also found that Patchy cells also showed almost no response to 2-heptanone in glomerulus DC3, consistent with our prediction that the individual dendritic tufts of a Patchy cell are compartmentalized, and hence, they should inherit the tuning of the PNs in their home glomerulus (Figures 3D and 3F). By contrast, we found that Full cells had robust calcium responses to 2-heptanone in DC3, supporting the conclusion that there is a spatial spread of voltage and/or calcium in these cells (Figures 3D and 3F).

Interestingly, we found that high concentrations of 2-heptanone suppressed the farnesol responses of Patchy cells in glomerulus DC3 (Figures 3D, 3F, and 3G). This may be due in part to the fact that a high concentration of 2-heptanone recruits intense activity in Full cells, driving widespread inhibition of ORN axon terminals, thereby decreasing ORN and PN activity in most glomeruli, and decreasing the excitatory drive onto Patchy cells. Moreover, some Patchy cells (subtype LN2P_c) receive substantial direct inhibitory input from Full cells (LN2F_b) (Figure 4A).

We observed a different result in Full cells. Here, adding 2-heptanone to farnesol boosted calcium signals in glomerulus DC3, rather than suppressing them (Figures 3D, 3F, and 3G). Both farnesol and 2-heptanone produced activity that spreads throughout the arbors of Full cells, and the effects of these two stimuli were approximately additive.

In summary, we find that Patchy cells are compartmentalized, whereas Full cells are much less compartmentalized. Patchy cell tufts are most effectively recruited by private odors. Meanwhile,

Please cite this article in press as: Barth-Maron et al., Interactions between specialized gain control mechanisms in olfactory processing, Current Biology (2023), https://doi.org/10.1016/j.cub.2023.10.041

CellPress
OPEN ACCESS

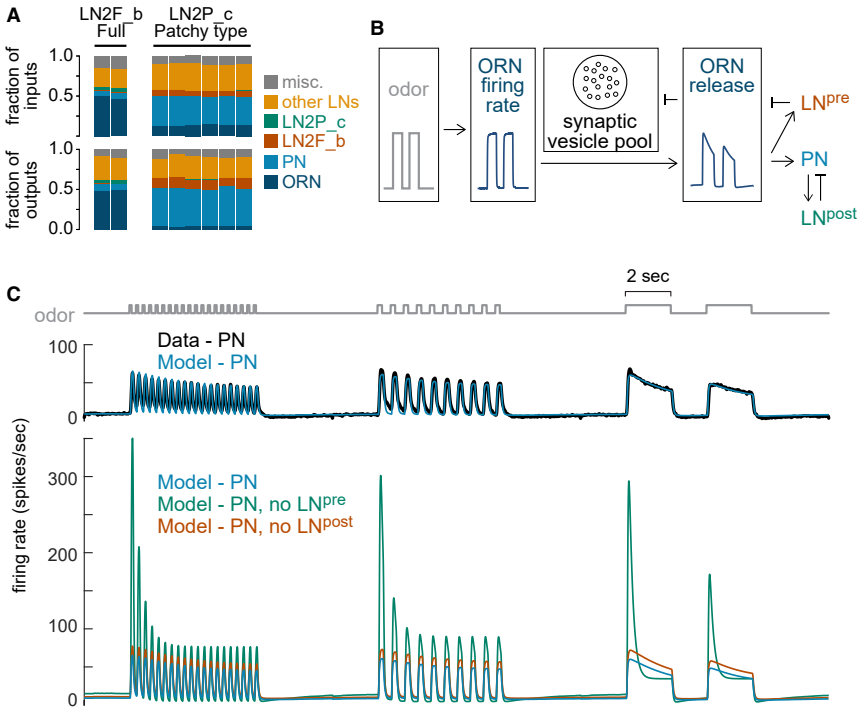

Figure 4. LNs specialized for pre- or post-synaptic gain control

(A) Fraction of input synapses and output synapses arising from different cell types, for both LN2F_b and LN2P_c cells. Other LNs comprise all other LN types, including other subtypes of Patchy cells. Miscellaneous cells include extrinsic inputs from other brain regions. Note that Full cells are strongly reciprocally connected with ORNs, whereas LN2P_c cells are reciprocally connected with PNs, with some ORN input as well.

(B) Model. The input to the model is a train of odor pulses. ORN firing rate is a smoothed version of this input. ORN firing rate is translated into ORN neurotransmitter release, which depends on the size of the available synaptic vesicle pool. ORN release depletes the available pool. ORNs excite PNs and LNs. LN^{pre} suppresses ORN release, whereas LN^{post} suppresses PN firing rate.

(C) With both LNs present, model parameters are fit to minimize the mean squared error between PN data and model output (R^2 = 0.849). Removing LN^{post} has no effect on PN dynamics, whereas removing LN^{pre} primarily disinhibits the transient PN onset response and the response to higher-frequency odor pulse trains.

Full cells are most effectively recruited by odors that elicit widespread input to many glomeruli.

LNs specialized for pre- or post-synaptic gain control

Notably, different LNs in this network select different targets. For example, Full cells (LN2F_b) preferentially target ORN axon terminals and receive most of their excitatory input from ORNs (Figure 4A). By contrast, other LN types preferentially target PNs and receive most of their excitatory input from PNs; this group of LNs includes LN2P_c, a Patchy cell type (Figures 4A and S1).

To predict the functional consequences of these specializations, we built a computational model comprising ORNs, PNs, and two LN types, one recurrently connected with ORNs (LN^{pre}) and the other recurrently connected with PNs (LN^{post}). These two LN types are designed to capture the basic features of LN2F_b and LN2P_c cells, respectively. For simplicity, this model focuses on one glomerulus, and each cell type is represented by one network node (Figure 4B). We added presynaptic inhibition to this model, following published works.[34] Specifically, we endowed model ORN synapses with short-term depression that grows with p,[35,36] and we modeled presynaptic inhibition as a decrease in p.[19] Meanwhile, we modeled postsynaptic inhibition as a subtractive effect on PN activity. We fit the parameters of this model to our electrophysiological data, and we then used this model to investigate how PN dynamics change when we perturb each LN type.

Initially, with both LN types present, we confirmed that this model generates realistic dynamics (Figure 4C) and that PNs are able to track odor concentration fluctuations over a wide range of temporal frequencies. When we turned off presynaptic inhibition, PN responses showed more temporal distortion—specifically, more prominent onset transients and more severe rundown during a pulse train. This is because in the absence of presynaptic inhibition, ORN release probability (p) was fixed at a high value, producing stronger short-term depression and thus more high-pass temporal filtering. When we instead turned off postsynaptic inhibition, PN dynamics were similar to what we observed in the intact model network, although response gain was increased.

In summary, short-term synaptic depression produces temporal distortion in the form of high-pass filtering. Our model predicts that presynaptic inhibition mitigates this distortion while also further controlling gain. Our model predicts that postsynaptic inhibition contributes to gain control, but without mitigating temporal distortion. We next set out to test these predictions experimentally.

Using optogenetic stimulation to test model predictions

To target individual LN types for stimulation, we expressed CsChrimson[37] under the control of our selective Gal4 lines. We then used light to optogenetically stimulate these cells while recording the odor responses of PNs in glomerulus DC3. Here, we used the private odor for DC3 (a low concentration of farnesol), and we synchronized light and odor so that light boosted odor-evoked depolarization in these LNs. We delivered odor pulses at three different frequencies and tested six different light intensities. For comparison, we also performed an equivalent experiment on the model.

We found that optogenetically activating Patchy cells inhibited PN odor responses with only relatively small changes to PN response dynamics (Figures 5A and 5B) or frequency tuning (Figures 5C and 5D). This resembles the effect of activating LN^{post} in the model. At the highest optogenetic stimulus intensities, activation of Patchy cells began to affect PN response

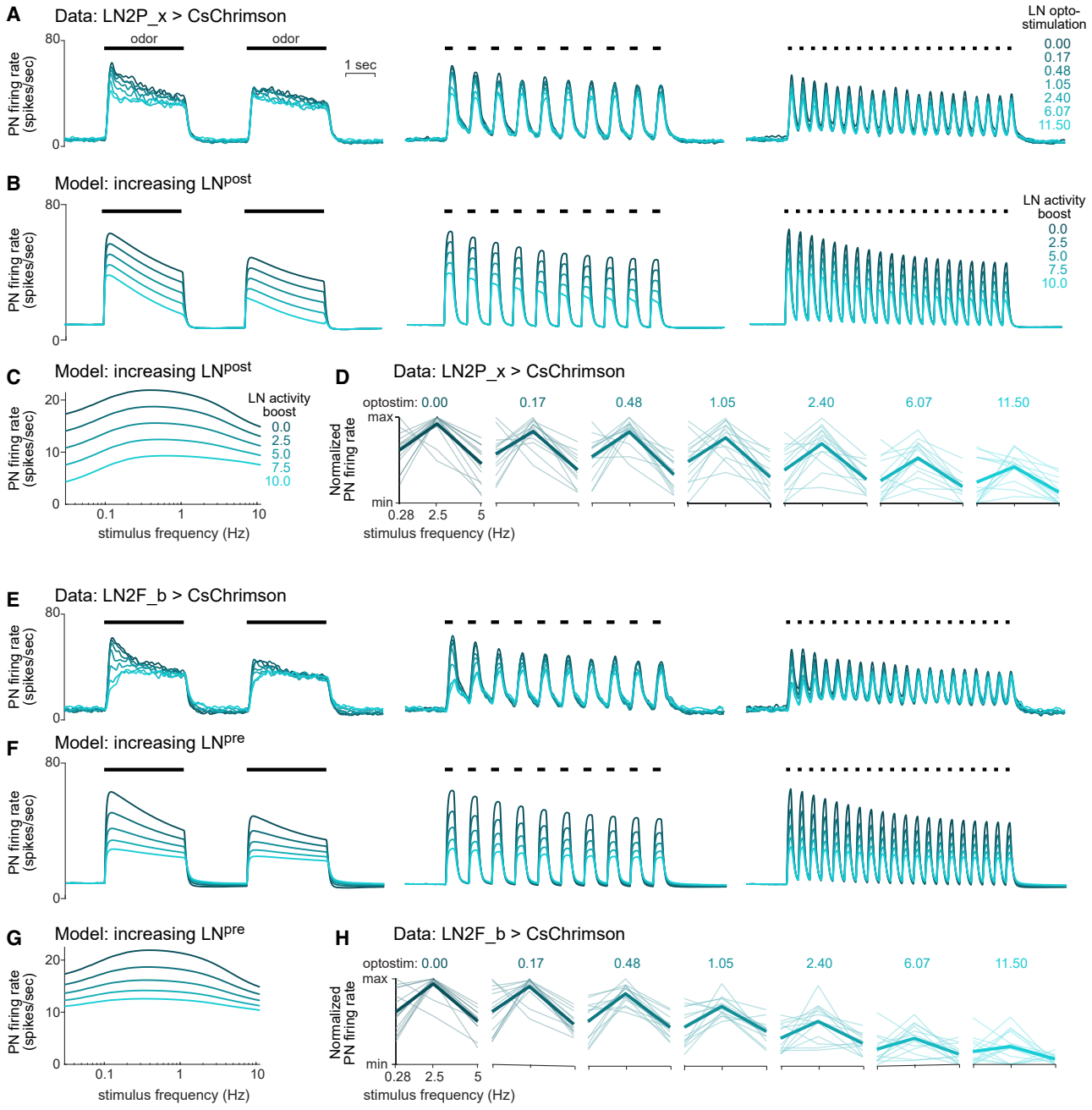

Figure 5. Using optogenetic stimulation to test model predictions

(A) Data: optogenetic activation of LN2P_x cells suppresses DC3 PN responses to a private odor (farnesol 10^{-5}). Firing rates were averaged across recorded PNs (n = 14) for each optostimulation level, ranging from 0.00 to 11.50 mW. Odor pulse frequencies were 0.28, 2.5, and 5 Hz. Optostimulation was synchronized with odor valve openings (black horizontal lines).

(B) Model PN firing rates with boosted activity in LN^{post}. Zero added activity represents the default model shown in Figure 4C. Values show activity injected at each time step (e.g., 2.5 Hz); due to the integrative properties of the LN, this resulted in an LN firing rate increase that was larger than these values. Activity injections were synchronized with the simulated odor pulse.

(C) Model: PN firing rate versus odor pulse frequency. Boosting activity in LN^{post} has little effect on PN frequency tuning. Firing rates here (and in all frequency tuning curves) are averaged over the entire period of the pulse train.

(D) Data: normalized PN firing rate at each stimulus frequency, for increasing optogenetic activation of LN2P_x cells. Thin lines are individual experiments, thick lines are mean. Activation of LN2P_x cells has little effect on PN frequency tuning. Two-way analysis of covariance (ANCOVA) shows a significant effect of stimulus frequency (factor, $p = 1.8 \times 10^{-33}$) and light intensity (covariate, $p = 5.3 \times 10^{-21}$), but with no significant interaction ($p = 0.093$); moreover, Tukey post hoc tests showed no significant differences in the slope of the light/response relationship for different stimulus frequencies (2.5 versus 0.28 Hz, $p = 0.452$; 2.5 versus 5 Hz, $p = 0.073$; 0.28 versus 5 Hz, $p = 0.586$).

(E) Same as (A) but for optogenetic activation of LN2F_b cells (n = 14).

(legend continued on next page)

Please cite this article in press as: Barth-Maron et al., Interactions between specialized gain control mechanisms in olfactory processing, Current Biology (2023), https://doi.org/10.1016/j.cub.2023.10.041

dynamics, but this effect was small. Thus, we provisionally conclude that our Patchy transgenic line drives Gal4 expression in LN2P_c cells, which primarily target PNs rather than ORNs (Figure 4A).

Conversely, we found that optogenetically activating Full cells inhibited PN odor responses with dramatic changes to PN response dynamics, making the PN response a more faithful copy of the odor stimulus (Figures 5E and 5F) by diminishing band-pass temporal filtering (Figures 5G and 5H). This result indicates that Full cells effectively reduce the temporal distortion arising from short-term synaptic depression, consistent with theoretical predictions.[19] This outcome resembles the effect of activating LN^{pre} in the model, which makes sense, given that Full cells make many output synapses to ORN terminals.

Next, we tested the effect of optogenetically suppressing Full cells, using the inhibitory opsin GtACR1.[38,39] In these experiments, we used a strong odor (2-heptanone 10^{-2}) to produce a strong excitatory drive to the network. We found that suppression of Full cells disinhibited PN responses at odor onset (Figure 6A), consistent with model predictions (Figure 6B); it also sharpened PN frequency tuning (Figure 6C), again consistent with model predictions (Figure 6D). Notably, these results are the opposite of what we observed when we optogenetically activated Full cells (Figures 5E–5H). As a negative control, we confirmed that suppressing Full cells has no effect on PN responses to a weak private odor (Figure S4).

Together, these results indicate that Patchy cells can inhibit network output without altering network dynamics. By contrast, Full cells do alter network dynamics, and they do so in a manner that promotes equal sensitivity to all stimulus frequencies. As a result, the dynamics of PN output more closely resemble the dynamics of odor input. It is notable that we see any effect of activating and suppressing Full cells, given that there are only two Full cells per hemisphere, of the ~200 LNs per hemisphere. This may be because these two Full cells alone are responsible for ~30% of all LN → ORN connections (Figure S1).

Comparing global and local inhibitions

Thus far, our results argue that gain control in the antennal lobe is mediated by at least two types of LNs, LN2P_c (Patchy) and LN2F_b (Full). The former mediates local postsynaptic inhibition, whereas the latter mediates global presynaptic inhibition (Figure 7A). Why would this arrangement be potentially useful?

To address this question, we should consider how signals from different olfactory glomeruli are combined at the level of downstream neurons (Figure 7B). Some of these downstream neurons generate selective responses to particular odors[40–45] by combining PN signals from multiple glomeruli, weighted by the strength of PN connections.[44–46] Each odor response (Figure 7C) can be interpreted as a vector in N-dimensional space, where N is the number of glomeruli. If a downstream neuron responds selectively to one odor, its weights define a hyperplane that separates that odor from all others. Linear separability is improved if all odor vectors have approximately the same distance from the origin (Figure 7D). We hypothesized that linear separability is increased by both global presynaptic inhibition and local postsynaptic inhibition.

To investigate this idea, we took advantage of a large published dataset of ORN odor responses.[6] We supplemented this dataset with a simulated private odor for each ORN type because some ORN types did not have private odors in the published dataset (Figure 7C). Next, we used a published model[47,48] to simulate the transformation from ORN firing rates to PN firing rates without inhibition (Figure 7E). We confirmed that these model PN responses are more linearly separable than ORN responses (Figure 7F), as reported previously.[47,48] This occurs because short-term synaptic depression at ORN → PN synapses tends to equalize PN population response magnitudes.

Next, we added global presynaptic inhibition to the model (Figure 7G). Specifically, we added an inhibitory unit that performs presynaptic inhibition on all ORNs, and we made its activity proportional to the summed activity of the entire ORN population (LN^{pre}). This further improves odor separability (Figure 7H), as reported previously,[47,48] because global presynaptic inhibition reduces saturation when total ORN activity is high.

Finally, we added local postsynaptic inhibition (Figure 7I). Specifically, we added an inhibitory unit, which is dedicated to each PN (LN^{post}) and which scales down the activity of that PN. We found that local postsynaptic inhibition produced a further improvement in linear separability (Figure 7J). Here, however, we only observed a notable improvement if our odor set contained strong private odors (Figure S5). Strong private odors are relatively untouched by global gain control because they do not drive much global activity. For these odors to recruit gain control, there needs to be local inhibition. Local gain control prevents these odors from generating false hits in off-target downstream classifiers.

To summarize, this model shows how odor discrimination can be improved by three gain control mechanisms acting in series. First, short-term synaptic depression at ORN → PN synapses reduces the strongest PN firing rates. Second, global presynaptic inhibition further reduces gain when total ORN activity is high. Finally, local postsynaptic inhibition limits PN responses to strong private odors that have escaped the effects of global inhibition. All three mechanisms tend to equalize PN population response magnitudes, thereby improving odor discrimination.

DISCUSSION

In this study, we asked how interneuron diversity contributes to gain control in olfactory processing. This question was motivated by the fact that there is a wide variety of interneuron types in the *Drosophila* antennal lobe,[10–19] just as in the vertebrate olfactory bulb,[24–27] but we do not understand how all these interneurons work together to perform gain control. Here, we focused on two types of inhibitory interneurons, and we show that they

(F and G) Same as (B) and (C) but with boosted activity in LN^{pre}, which flattens PN frequency tuning.

(H) Same as (D) but for increasing optogenetic activation of LN2F_b cells, which flattens PN frequency tuning. Two-way ANCOVA shows a significant effect of stimulus frequency (factor, $p = 1.9 \times 10^{-25}$) and light intensity (covariate, $p = 7.5 \times 10^{-44}$) with a significant interaction ($p = 4.4 \times 10^{-4}$). Tukey post hoc tests showed several significant differences in the slope of the light/response relationship for different stimulus frequencies (2.5 versus 0.28 Hz, $p = 2.5 \times 10^{-3}$; 2.5 versus 5 Hz, $p = 1.1 \times 10^{-3}$; 0.28 versus 5 Hz, $p = 0.971$).

Please cite this article in press as: Barth-Maron et al., Interactions between specialized gain control mechanisms in olfactory processing, Current Biology (2023), https://doi.org/10.1016/j.cub.2023.10.041

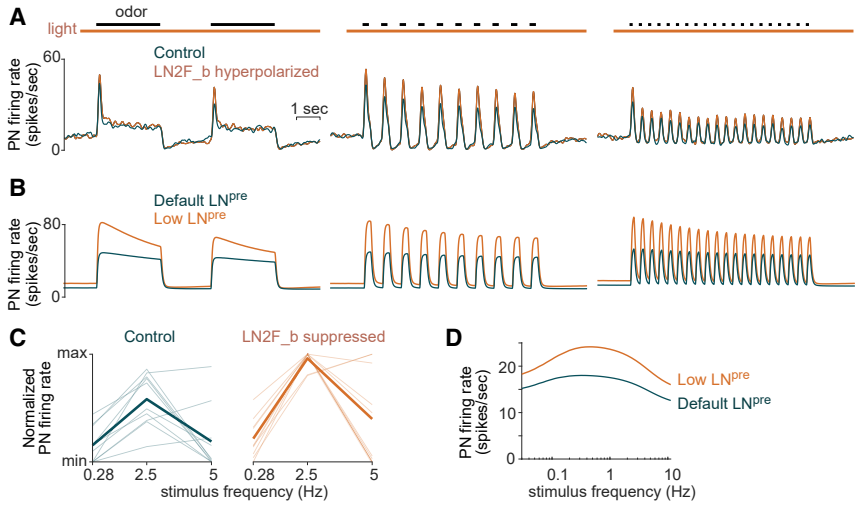

Figure 6. Using optogenetic suppression to test model predictions

(A) Data: optogenetic suppression of LN2F_b cells disinhibits PN odor responses. All recorded PNs were in glomerulus DC3. The odor was a stimulus that drives strong activity in a broad population of ORNs (2-heptanone 10^{-2}). PN firing rates were averaged across recorded cells (n = 11 PNs). Odor pulse frequencies were 0.28, 2.5, and 5 Hz. Light was turned on before the odor pulse train, and terminated after the end of the odor pulse train. We chose to begin suppressing LN activity before odor onset because LN activity before odor onset can alter PN responses to a subsequent odor.[19]

(B) Model PN firing rates with lowered activity in LN^{pre}, compared with the default level of activity. Activity in LN^{pre} was lowered throughout the stimulation. Note that lowering LN^{pre} preferentially disinhibits the onset of the PN odor response, and this resembles the effect of suppressing activity in LN2F_b cells.

(C) Data: normalized PN firing rate at each stimulus frequency, with and without optogenetic suppression of LN2F_b cells. Suppressing LN2F_b sharpens PN frequency tuning. The effect of light is significant in a mixed-effects ANOVA ($p = 1.80 \times 10^{-3}$), and there is a significant interaction between light and odor pulse frequency ($p = 1.30 \times 10^{-3}$). Thin lines are individual cells, and thick lines are mean.

(D) Model: PN firing rate versus odor pulse frequency. Lowering activity in LN^{pre} sharpens PN frequency tuning.

See also Figure S4.

play different functional roles. Our results show how inhibitory interneurons can work together to minimize temporal distortions while improving stimulus discrimination.

Specialized properties of inhibitory interneurons

Here, we show that Patchy cells are nonspiking cells that use graded potentials for signaling. Moreover, their odor-evoked calcium signals are largely confined to individual dendritic tufts. Thus, each tuft can be treated as a separate gain control unit. Similarly, a recent study reported that specific cells in the *Drosophila* visual system also have distinct tufts that are functionally compartmentalized.[49] Our results imply that Patchy cells are specialized to perform intra-glomerular gain control. However, a widespread odor stimulus can actually suppress local calcium signals in Patchy cell dendrites; thus, Patchy cells should be most efficiently recruited by an odor stimulus that evokes input to just a few glomeruli. Functionally, Patchy cells may be analogous to the nonspiking periglomerular cells of the vertebrate olfactory bulb, which are specialized for intra-glomerular inhibition.[24,50] They may also be functionally similar to LNs reported in other insect species that seem to be electrically compartmentalized[51] and lack Na^+ spikes,[52–56] although they do not have a distinctive Patchy morphology.

Meanwhile, we found that Full cells are specialized for global presynaptic inhibition. Odor responses spread throughout the arbor of each Full cell, so that even focal inputs generate global signals. Full cells primarily target ORN axon terminals and are responsible for a large fraction of all LN → ORN synapses. We showed that activating these cells increases presynaptic inhibition, whereas hyperpolarizing them decreases presynaptic inhibition. Full cells may be analogous to specific inhibitory SA cells of the vertebrate olfactory bulb. SA cells can have multiple axons that contact many glomeruli,[57,58] and they broadcast focal olfactory input throughout the olfactory bulb, recruiting widespread inhibition.[59,60] SA cells form reciprocal connections with external tufted cells, which relay much of the excitation that projections neurons receive from ORNs; thus, SA cells control the input to PNs, analogous to the function of Full cells in *Drosophila*.

We chose to focus our attention here on Patchy and Broad LNs because these comprise the majority of LN output synapses[3] (Figure S1). However, there are also many distinct regional and sparse LN types with stereotyped morphology and dedicated axonal and dendritic regions.[3] These regional and sparse LN types may mediate specific interactions between pairs or subsets of glomeruli.[61,62]

Interactions among gain control mechanisms

Our findings indicate that the antennal lobe contains at least three gain control mechanisms. The first is short-term synaptic depression at ORN → PN synapses.[8] The second is broad presynaptic inhibition.[35] The third is intra-glomerular inhibition, which is at least partly postsynaptic.[9,10,35] Our results reveal how these mechanisms interact to manage tradeoffs in network function.

First, short-term synaptic depression operates on the smallest spatial scale, at the level of single ORN → PN synapses.[8] Short-term synaptic depression effectively limits postsynaptic responses when presynaptic firing rates are high.[19,35,36,63,64] However, it also causes distortion: it accentuates responses to odor onset, while also creating a "peaky" frequency tuning profile. This is a problem if PNs need to be equally sensitive to all stimuli, regardless of their frequency. Although there is evidence that some PNs extract specific frequency features from an odor stimulus waveform,[65] it may still be useful to minimize distortions in the temporal input to a typical PN. In the future, it would be interesting to see whether PNs with specialized frequency filtering properties have specialized LN inputs.

Presynaptic inhibition mitigates this problem by reducing release probability (p_r), thereby reducing short-term depression, hence reducing distortion. It is important that this process is

Please cite this article in press as: Barth-Maron et al., Interactions between specialized gain control mechanisms in olfactory processing, Current Biology (2023), https://doi.org/10.1016/j.cub.2023.10.041

CellPress
OPEN ACCESS

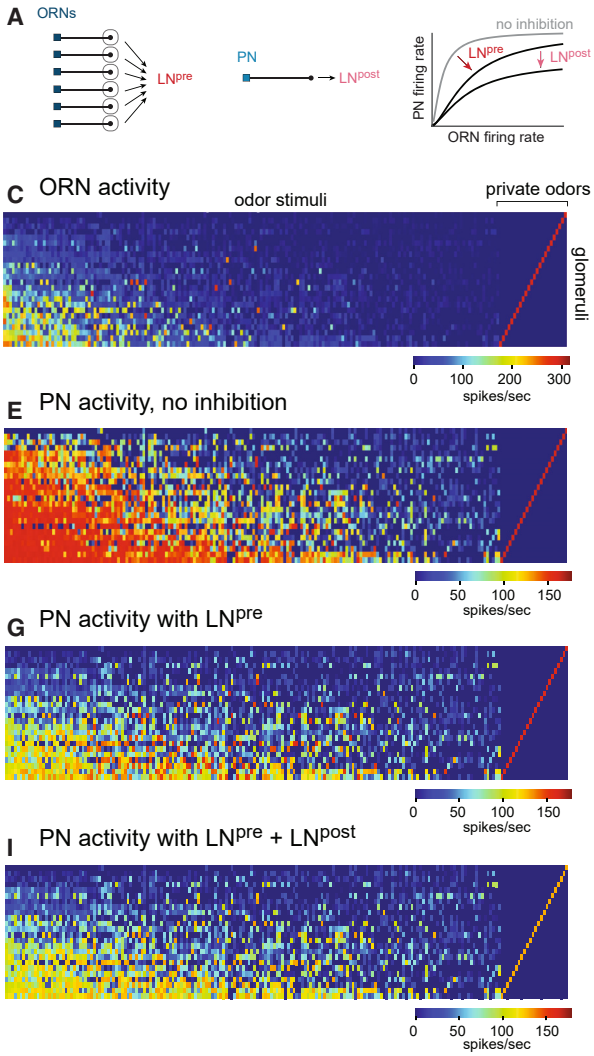

Figure 7. Comparing global and local inhibition

(A) We implemented a multiglomerular model where LN^{pre} cells pool ORN input from all glomeruli, and LN^{post} cells receive PN input from individual glomeruli. LN^{pre} scales ORN input to each glomerulus, whereas LN^{post} scales PN output from each glomerulus.

(B) Downstream LHNs pool input from multiple glomeruli.

(C) A dataset of ORN odor responses, supplemented with simulated private odors for each glomerulus.

(D) Each odor can be schematized as a vector in glomerular coding space. Different presentations of the same odor elicit slightly different responses (circles); nonetheless, we can draw a boundary that separates each odor from the rest (dashed lines). Linear separability is maximized if all vectors have the same distance from the origin.

(E) Modeled PN responses with no inhibition.

(F) Accuracy of linear classifiers trained to selectively recognize each odor. Classifiers were trained separately on ORN responses or PN responses. Each symbol is an odor, with private odors in red. Almost every odor lies above the line of unity (black line), meaning that classification is improved by the ORN → PN transformation.

(G) Modeled PN responses with LN^{pre}.

(H) Accuracy of linear classifiers trained on PN responses with no inhibition, versus PN responses with LN^{pre}. For almost every odor, classification is improved by global presynaptic inhibition.

(I) Modeled PN responses with LN^{pre} and LN^{post}.

(J) Accuracy of linear classifiers trained on PN responses with LN^{pre}, versus PN responses with LN^{pre} and LN^{post}. For almost every odor, classification is improved by local postsynaptic inhibition. Classification accuracy decreases for the simulated private odors.

See also Figure S5.

dynamic: if p_r were low at all times, then weak postsynaptic responses could be lost in the barrage of network noise.[66] In effect, global presynaptic inhibition manages the conflict between the need for temporal fidelity (avoiding distortion) and the need for sensitivity (maintaining large responses). Temporal fidelity is favored by low p_r, whereas sensitivity is favored by high p_r. Presynaptic inhibition manages this tradeoff by lowering p_r only when stimuli are intense.

Importantly, our results argue that presynaptic inhibition in this system is primarily a global phenomenon. Unlike short-term synaptic depression, which operates on a small spatial scale, presynaptic inhibition is mediated by inhibitory interneurons with widespread arbors. Each of these inhibitory interneuron pools ORN input from most or all glomeruli, allowing it to generate a better prediction of the network's signal-to-noise ratio, even on short time scales. This can be seen as a form of predictive coding[67]: the current level of sensory input to all glomeruli is taken as a prediction of the activity that each glomerulus will see in the near future because strong sensory input to any given glomerulus often correlates with strong input to multiple glomeruli.[6,68] When multiple glomeruli are receiving strong input, then p_r can be safely lowered.

Finally, intra-glomerular inhibition implements gain control for stimuli that activate just one glomerulus or a few glomeruli. These stimuli require a gain control mechanism that integrates input over a small spatial scale, and the compartmentalized tufts of Patchy cells satisfy this need. In principle, intra-glomerular inhibition can be either postsynaptic or presynaptic. The Patchy cells we have focused on (likely LN2P_c) implement primarily postsynaptic inhibition, but other Patchy types (LN2P_a and LN2P_b) are positioned to implement a mixture of post- and pre-synaptic inhibitions.

Importantly, these three mechanisms of gain control inhibit each other. Short-term synaptic depression reduces the recruitment of LNs[18,19] and thus should reduce all forms of inhibition; conversely, presynaptic inhibition reduces short-term synaptic depression.[34,69] Moreover, in this study, we showed that global presynaptic inhibition suppresses the local calcium signals in Patchy cells, which should reduce local postsynaptic inhibition. These competitive interactions between different mechanisms

of gain control ought to limit the total amount of gain control in the network. Competition also changes the properties of gain control to suit the current needs of the system; for instance, it may favor sensitivity when a background odor is present, while favoring temporal fidelity when odors co-fluctuate as if originating from a single source (Figure S6).

Benefits of gain control

Gain control in this network is potentially useful for several reasons. First, gain control limits metabolic costs by attenuating the high firing rates in output neurons. Higher firing rates typically transmit less information per spike.[70] Thus, keeping firing rates low can be a way to maximize the information transmitted per spike. All three mechanisms of gain control should limit postsynaptic spikes, and hence, they should all be useful for this reason.

Second, gain control can promote high sensitivity over a wide dynamic range, thereby making stimuli more discriminable by downstream neurons.[47,48,71,72] Specifically, previous modeling work has shown that short-term synaptic depression should improve odor discrimination, and adding global presynaptic inhibition should produce a further improvement.[47,48] Here, we extend this model to show that there is a further improvement in odor discrimination if we add intra-glomerular postsynaptic inhibition to the network. In all three cases, the reason is the same: all three forms of gain control tend to equalize population response magnitudes for different stimuli. This in turn makes it easier to find a set of synaptic weights that allow a downstream neuron to respond selectively to a particular odor stimulus.

Although this study has focused on one specific network in the *Drosophila* olfactory system, our results have general implications. Gain control is a ubiquitous phenomenon in every sensory system. Moreover, the gain control model we fit to our data in this study is an extension of the "divisive normalization" formalism that is widely used to describe transformations in visual cortex and other sensory systems.[73] Our model shows how that formalism can be extended to include multiple gain control mechanisms that are chained together in series. Our work makes testable predictions for how other biological neural networks might use a similar architecture to achieve robust network performance.

STAR★METHODS

Detailed methods are provided in the online version of this paper and include the following:

- KEY RESOURCES TABLE
- RESOURCE AVAILABILITY
  - Lead contact
  - Materials availability
  - Data and code availability
- EXPERIMENTAL MODEL AND STUDY PARTICIPANT DETAILS
  - Fly husbandry and genotypes
  - Origins of transgenic stocks
- METHOD DETAILS
  - Experimental design
  - MultiColor FlpOut
  - Odor delivery
  - Stimuli
  - Fly preparation
  - Electrophysiology
  - Optogenetics
  - Calcium imaging
  - *In vivo* neuropil staining
- QUANTIFICATION AND STATISTICAL ANALYSIS
  - Connectomics analysis
  - Electrophysiology data analysis
  - Calcium imaging data analysis
  - Statistical analysis
  - Dynamical model
  - Population activity model

SUPPLEMENTAL INFORMATION

Supplemental information can be found online at https://doi.org/10.1016/j.cub.2023.10.041.

ACKNOWLEDGMENTS

We are grateful to Stephen Plaza, Lou Scheffer, Jane Anne Horne, and Ian Meinertzhagen for advice on pilot analyses of other connectome data, prior to the availability of the hemibrain dataset. We are grateful to Barret Pfeiffer and Gerry Rubin for providing fly stocks. This work was funded by grants from the NIH (F31 DC016196 to A.B.-M. and R01 DC008174 to R.I.W.). R.I.W. is an Investigator of the Howard Hughes Medical Institute. This work was also supported by the Bloomington Drosophila Stock Center (NIH P40 OD018537), the Harvard Medical School Neurobiology Imaging Facility (NIH P30 NS072030), and the HMS Research Instrumentation Core Facility.

AUTHOR CONTRIBUTIONS

A.B.-M. performed electrophysiology and calcium imaging experiments, data analysis, and computational modeling. I.D. generated MCFO images. A.B.-M. and R.I.W. together designed the study and wrote the manuscript.

DECLARATION OF INTERESTS

A.B.-M. is currently an employee of Neumora Therapeutics, Inc.

Received: April 7, 2023
Revised: August 16, 2023
Accepted: October 23, 2023
Published: November 14, 2023

REFERENCES

1. Rieke, F., and Rudd, M.E. (2009). The challenges natural images pose for visual adaptation. Neuron *64*, 605–616.
2. Weber, A.I., Krishnamurthy, K., and Fairhall, A.L. (2019). Coding principles in adaptation. Annu. Rev. Vis. Sci. *5*, 427–449.
3. Schlegel, P., Bates, A.S., Stürner, T., Jagannathan, S.R., Drummond, N., Hsu, J., Serratosa Capdevila, L., Javier, A., Marin, E.C., Barth-Maron, A., et al. (2021). Information flow, cell types and stereotypy in a full olfactory connectome. eLife *10*, e66018. https://doi.org/10.7554/eLife.66018.
4. Diamond, J.S. (2017). Inhibitory interneurons in the retina: types, circuitry, and function. Annu. Rev. Vis. Sci. *3*, 1–24.
5. Drew, P.J., and Abbott, L.F. (2006). Models and properties of power-law adaptation in neural systems. J. Neurophysiol. *96*, 826–833.
6. Hallem, E.A., and Carlson, J.R. (2006). Coding of odors by a receptor repertoire. Cell *125*, 143–160.
7. Nagel, K.I., and Wilson, R.I. (2011). Biophysical mechanisms underlying olfactory receptor neuron dynamics. Nat. Neurosci. *14*, 208–216.

8. Kazama, H., and Wilson, R.I. (2008). Homeostatic matching and nonlinear amplification at identified central synapses. Neuron *58*, 401–413.
9. Liu, W.W., and Wilson, R.I. (2013). Glutamate is an inhibitory neurotransmitter in the Drosophila olfactory system. Proc. Natl. Acad. Sci. USA *110*, 10294–10299.
10. Yaksi, E., and Wilson, R.I. (2010). Electrical coupling between olfactory glomeruli. Neuron *67*, 1034–1047.
11. Wilson, R.I., Turner, G.C., and Laurent, G. (2004). Transformation of olfactory representations in the *Drosophila* antennal lobe. Science *303*, 366–370.
12. Wilson, R.I., and Laurent, G. (2005). Role of GABAergic inhibition in shaping odor-evoked spatiotemporal patterns in the *Drosophila* antennal lobe. J. Neurosci. *25*, 9069–9079.
13. Shang, Y., Claridge-Chang, A., Sjulson, L., Pypaert, M., and Miesenböck, G. (2007). Excitatory local circuits and their implications for olfactory processing in the fly antennal lobe. Cell *128*, 601–612.
14. Okada, R., Awasaki, T., and Ito, K. (2009). Gamma-aminobutyric acid (GABA)-mediated neural connections in the Drosophila antennal lobe. J. Comp. Neurol. *514*, 74–91.
15. Chou, Y.H., Spletter, M.L., Yaksi, E., Leong, J.C., Wilson, R.I., and Luo, L. (2010). Diversity and wiring variability of olfactory local interneurons in the Drosophila antennal lobe. Nat. Neurosci. *13*, 439–449.
16. Seki, Y., Rybak, J., Wicher, D., Sachse, S., and Hansson, B.S. (2010). Physiological and morphological characterization of local interneurons in the Drosophila antennal lobe. J. Neurophysiol. *104*, 1007–1019.
17. Huang, J., Zhang, W., Qiao, W., Hu, A., and Wang, Z. (2010). Functional connectivity and selective odor responses of excitatory local interneurons in Drosophila antennal lobe. Neuron *67*, 1021–1033.
18. Nagel, K.I., and Wilson, R.I. (2016). Mechanisms underlying population response dynamics in inhibitory interneurons of the Drosophila antennal lobe. J. Neurosci. *36*, 4325–4338.
19. Nagel, K.I., Hong, E.J., and Wilson, R.I. (2015). Synaptic and circuit mechanisms promoting broadband transmission of olfactory stimulus dynamics. Nat. Neurosci. *18*, 56–65.
20. Scheffer, L.K., Xu, C.S., Januszewski, M., Lu, Z., Takemura, S.Y., Hayworth, K.J., Huang, G.B., Shinomiya, K., Maitlin-Shepard, J., Berg, S., et al. (2020). A connectome and analysis of the adult Drosophila central brain. eLife *9*, e57443. https://doi.org/10.7554/eLife.57443.
21. Zheng, Z., Lauritzen, J.S., Perlman, E., Robinson, C.G., Nichols, M., Milkie, D., Torrens, O., Price, J., Fisher, C.B., Sharifi, N., et al. (2018). A complete electron microscopy volume of the brain of adult Drosophila melanogaster. Cell *174*, 730–743.e22.
22. Horne, J.A., Langille, C., McLin, S., Wiederman, M., Lu, Z., Xu, C.S., Plaza, S.M., Scheffer, L.K., Hess, H.F., and Meinertzhagen, I.A. (2018). A resource for the Drosophila antennal lobe provided by the connectome of glomerulus VA1v. eLife *7*, e37550. https://doi.org/10.7554/eLife.37550.
23. Berck, M.E., Khandelwal, A., Claus, L., Hernandez-Nunez, L., Si, G., Tabone, C.J., Li, F., Truman, J.W., Fetter, R.D., Louis, M., et al. (2016). The wiring diagram of a glomerular olfactory system. eLife *5*, e14859. https://doi.org/10.7554/eLife.14859.
24. Ennis, M., Puche, A.C., Holy, T., and Shipley, M.T. (2015). The olfactory system. In The Rat Nervous System (Academic Press), pp. 761–803. https://doi.org/10.1016/b978-0-12-374245-2.00027-9.
25. Wachowiak, M., and Shipley, M.T. (2006). Coding and synaptic processing of sensory information in the glomerular layer of the olfactory bulb. Semin. Cell Dev. Biol. *17*, 411–423.
26. Burton, S.D. (2017). Inhibitory circuits of the mammalian main olfactory bulb. J. Neurophysiol. *118*, 2034–2051.
27. Nagayama, S., Homma, R., and Imamura, F. (2014). Neuronal organization of olfactory bulb circuits. Front. Neural Circuits *8*, 98.
28. Nern, A., Pfeiffer, B.D., and Rubin, G.M. (2015). Optimized tools for multicolor stochastic labeling reveal diverse stereotyped cell arrangements in the fly visual system. Proc. Natl. Acad. Sci. USA *112*, E2967–E2976.
29. Tanaka, N.K., Endo, K., and Ito, K. (2012). Organization of antennal lobe-associated neurons in adult Drosophila melanogaster brain. J. Comp. Neurol. *520*, 4067–4130.
30. Lai, S.L., Awasaki, T., Ito, K., and Lee, T. (2008). Clonal analysis of Drosophila antennal lobe neurons: diverse neuronal architectures in the lateral neuroblast lineage. Development *135*, 2883–2893.
31. Eckstein, N., Bates, A.S., Du, M., Hartenstein, V., Jefferis, G.S.X.E., and Funke, J. (2020). Neurotransmitter classification from electron microscopy images at synaptic sites in Drosophila. Preprint at bioRxiv. https://doi.org/10.1101/2020.06.12.148775.
32. Münch, D., and Galizia, C.G. (2016). DoOR 2.0–comprehensive mapping of Drosophila melanogaster odorant responses. Sci. Rep. *6*, 21841.
33. Ronderos, D.S., Lin, C.C., Potter, C.J., and Smith, D.P. (2014). Farnesol-detecting olfactory neurons in Drosophila. J. Neurosci. *34*, 3959–3968.
34. Olsen, S.R., and Wilson, R.I. (2008). Lateral presynaptic inhibition mediates gain control in an olfactory circuit. Nature *452*, 956–960.
35. Abbott, L.F., Varela, J.A., Sen, K., and Nelson, S.B. (1997). Synaptic depression and cortical gain control. Science *275*, 220–224.
36. Tsodyks, M.V., and Markram, H. (1997). The neural code between neocortical pyramidal neurons depends on neurotransmitter release probability. Proc. Natl. Acad. Sci. USA *94*, 719–723.
37. Klapoetke, N.C., Murata, Y., Kim, S.S., Pulver, S.R., Birdsey-Benson, A., Cho, Y.K., Morimoto, T.K., Chuong, A.S., Carpenter, E.J., Tian, Z., et al. (2014). Independent optical excitation of distinct neural populations. Nat. Methods *11*, 338–346.
38. Mohammad, F., Stewart, J.C., Ott, S., Chlebikova, K., Chua, J.Y., Koh, T.W., Ho, J., and Claridge-Chang, A. (2017). Optogenetic inhibition of behavior with anion channelrhodopsins. Nat. Methods *14*, 271–274.
39. Govorunova, E.G., Sineshchekov, O.A., Janz, R., Liu, X., and Spudich, J.L. (2015). NEUROSCIENCE. Natural light-gated anion channels: a family of microbial rhodopsins for advanced optogenetics. Science *349*, 647–650.
40. Wang, Y., Guo, H.F., Pologruto, T.A., Hannan, F., Hakker, I., Svoboda, K., and Zhong, Y. (2004). Stereotyped odor-evoked activity in the mushroom body of *Drosophila* revealed by green fluorescent protein-based Ca2+ imaging. J. Neurosci. *24*, 6507–6514.
41. Turner, G.C., Bazhenov, M., and Laurent, G. (2008). Olfactory representations by Drosophila mushroom body neurons. J. Neurophysiol. *99*, 734–746.
42. Perez-Orive, J., Mazor, O., Turner, G.C., Cassenaer, S., Wilson, R.I., and Laurent, G. (2002). Oscillations and sparsening of odor representations in the mushroom body. Science *297*, 359–365.
43. Murthy, M., Fiete, I., and Laurent, G. (2008). Testing odor response stereotypy in the Drosophila mushroom body. Neuron *59*, 1009–1023.
44. Frechter, S., Bates, A.S., Tootoonian, S., Dolan, M.J., Manton, J., Jamasb, A.R., Kohl, J., Bock, D., and Jefferis, G. (2019). Functional and anatomical specificity in a higher olfactory centre. eLife *8*, e44590.
45. Jeanne, J.M., Fişek, M., and Wilson, R.I. (2018). The organization of projections from olfactory glomeruli onto higher-order neurons. Neuron *98*, 1198–1213.e6.
46. Fişek, M., and Wilson, R.I. (2014). Stereotyped connectivity and computations in higher-order olfactory neurons. Nat. Neurosci. *17*, 280–288.
47. Olsen, S.R., Bhandawat, V., and Wilson, R.I. (2010). Divisive normalization in olfactory population codes. Neuron *66*, 287–299.
48. Luo, S.X., Axel, R., and Abbott, L.F. (2010). Generating sparse and selective third-order responses in the olfactory system of the fly. Proc. Natl. Acad. Sci. USA *107*, 10713–10718.
49. Meier, M., and Borst, A. (2019). Extreme compartmentalization in a Drosophila amacrine cell. Curr. Biol. *29*, 1545–1550.e2.
50. Bufler, J., Zufall, F., Franke, C., and Hatt, H. (1992). Patch-clamp recordings of spiking and nonspiking interneurons from rabbit olfactory bulb slices: membrane properties and ionic currents. J. Comp. Physiol. A *170*, 145–152.

51. Fusca, D., and Kloppenburg, P. (2021). Task-specific roles of local interneurons for inter- and intraglomerular signaling in the insect antennal lobe. eLife *10*, e65217. https://doi.org/10.7554/eLife.65217.

52. Fuscà, D., and Kloppenburg, P. (2021). Odor processing in the cockroach antennal lobe-the network components. Cell Tissue Res. *383*, 59–73.

53. Husch, A., Paehler, M., Fusca, D., Paeger, L., and Kloppenburg, P. (2009). Calcium current diversity in physiologically different local interneuron types of the antennal lobe. J. Neurosci. *29*, 716–726.

54. Husch, A., Paehler, M., Fusca, D., Paeger, L., and Kloppenburg, P. (2009). Distinct electrophysiological properties in subtypes of nonspiking olfactory local interneurons correlate with their cell type-specific Ca2+ current profiles. J. Neurophysiol. *102*, 2834–2845.

55. Tabuchi, M., Dong, L., Inoue, S., Namiki, S., Sakurai, T., Nakatani, K., and Kanzaki, R. (2015). Two types of local interneurons are distinguished by morphology, intrinsic membrane properties, and functional connectivity in the moth antennal lobe. J. Neurophysiol. *114*, 3002–3013.

56. Laurent, G., and Davidowitz, H. (1994). Encoding of olfactory information with oscillating neural assemblies. Science *265*, 1872–1875.

57. Aungst, J.L., Heyward, P.M., Puche, A.C., Karnup, S.V., Hayar, A., Szabo, G., and Shipley, M.T. (2003). Centre-surround inhibition among olfactory bulb glomeruli. Nature *426*, 623–629.

58. Kiyokage, E., Pan, Y.Z., Shao, Z., Kobayashi, K., Szabo, G., Yanagawa, Y., Obata, K., Okano, H., Toida, K., Puche, A.C., et al. (2010). Molecular identity of periglomerular and short axon cells. J. Neurosci. *30*, 1185–1196.

59. Banerjee, A., Marbach, F., Anselmi, F., Koh, M.S., Davis, M.B., Garcia da Silva, P., Delevich, K., Oyibo, H.K., Gupta, P., Li, B., et al. (2015). An interglomerular circuit gates glomerular output and implements gain control in the mouse olfactory bulb. Neuron *87*, 193–207.

60. Burton, S.D., LaRocca, G., Liu, A., Cheetham, C.E.J., and Urban, N.N. (2017). Olfactory bulb deep short-axon cells mediate widespread inhibition of tufted cell apical dendrites. J. Neurosci. *37*, 1117–1138.

61. Vogt, K., Zimmerman, D.M., Schlichting, M., Hernandez-Nunez, L., Qin, S., Malacon, K., Rosbash, M., Pehlevan, C., Cardona, A., and Samuel, A.D.T. (2021). Internal state configures olfactory behavior and early sensory processing in Drosophila larvae. Sci. Adv. *7*, https://doi.org/10.1126/sciadv.abd6900.

62. Silbering, A.F., and Galizia, C.G. (2007). Processing of odor mixtures in the Drosophila antennal lobe reveals both global inhibition and glomerulus-specific interactions. J. Neurosci. *27*, 11966–11977.

63. Dunn, F.A., Doan, T., Sampath, A.P., and Rieke, F. (2006). Controlling the gain of rod-mediated signals in the mammalian retina. J. Neurosci. *26*, 3959–3970.

64. Oesch, N.W., and Diamond, J.S. (2011). Ribbon synapses compute temporal contrast and encode luminance in retinal rod bipolar cells. Nat. Neurosci. *14*, 1555–1561.

65. Taisz, I., Donà, E., Münch, D., Bailey, S.N., Morris, B.J., Meechan, K.I., Stevens, K.M., Varela-Martínez, I., Gkantia, M., Schlegel, P., et al. (2023). Generating parallel representations of position and identity in the olfactory system. Cell *186*, 2556–2573.e22.

66. Kazama, H., and Wilson, R.I. (2009). Origins of correlated activity in an olfactory circuit. Nat. Neurosci. *12*, 1136–1144.

67. Srinivasan, M.V., Laughlin, S.B., and Dubs, A. (1982). Predictive coding: a fresh view of inhibition in the retina. Proc. R. Soc. Lond. B Biol. Sci. *216*, 427–459.

68. Haddad, R., Weiss, T., Khan, R., Nadler, B., Mandairon, N., Bensafi, M., Schneidman, E., and Sobel, N. (2010). Global features of neural activity in the olfactory system form a parallel code that predicts olfactory behavior and perception. J. Neurosci. *30*, 9017–9026.

69. Zucker, R.S., and Regehr, W.G. (2002). Short-term synaptic plasticity. Annu. Rev. Physiol. *64*, 355–405.

70. Sterling, P., and Laughlin, S. (2015). Principles of Neural Design (MIT Press).

71. Ringach, D.L. (2010). Population coding under normalization. Vision Res. *50*, 2223–2232.

72. DiCarlo, J.J., and Cox, D.D. (2007). Untangling invariant object recognition. Trends Cogn. Sci. *11*, 333–341.

73. Carandini, M., and Heeger, D.J. (2011). Normalization as a canonical neural computation. Nat. Rev. Neurosci. *13*, 51–62.

74. Pfeiffer, B.D., Ngo, T.T., Hibbard, K.L., Murphy, C., Jenett, A., Truman, J.W., and Rubin, G.M. (2010). Refinement of tools for targeted gene expression in *Drosophila*. Genetics *186*, 735–755.

75. Pfeiffer, B.D., Jenett, A., Hammonds, A.S., Ngo, T.T., Misra, S., Murphy, C., Scully, A., Carlson, J.W., Wan, K.H., Laverty, T.R., et al. (2008). Tools for neuroanatomy and neurogenetics in *Drosophila*. Proc. Natl. Acad. Sci. USA *105*, 9715–9720.

76. Jenett, A., Rubin, G.M., Ngo, T.T., Shepherd, D., Murphy, C., Dionne, H., Pfeiffer, B.D., Cavallaro, A., Hall, D., Jeter, J., et al. (2012). A GAL4-driver line resource for Drosophila neurobiology. Cell Rep. *2*, 991–1001.

77. Dana, H., Sun, Y., Mohar, B., Hulse, B.K., Kerlin, A.M., Hasseman, J.P., Tsegaye, G., Tsang, A., Wong, A., Patel, R., et al. (2019). High-performance calcium sensors for imaging activity in neuronal populations and microcompartments. Nat. Methods *16*, 649–657.

78. Sutcliffe, B., Ng, J., Auer, T.O., Pasche, M., Benton, R., Jefferis, G.S., and Cachero, S. (2017). Second-generation *Drosophila* chemical tags: sensitivity, versatility, and speed. Genetics *205*, 1399–1408.

79. Pologruto, T.A., Sabatini, B.L., and Svoboda, K. (2003). ScanImage: flexible software for operating laser scanning microscopes. Biomed. Eng. OnLine *2*, 13.

80. Pnevmatikakis, E.A., and Giovannucci, A. (2017). NoRMCorre: an online algorithm for piecewise rigid motion correction of calcium imaging data. J. Neurosci. Methods *291*, 83–94.

81. Berg, S., and Schlegel, P. (2022). connectome-neuprint/neuprint-python: maintenance release. Zenodo. https://doi.org/10.5281/zenodo.7592899.

82. Gouwens, N.W., and Wilson, R.I. (2009). Signal propagation in Drosophila central neurons. J. Neurosci. *29*, 6239–6249.

83. Fisher, Y.E., Lu, J., D'Alessandro, I., and Wilson, R.I. (2019). Sensorimotor experience remaps visual input to a heading-direction network. Nature *576*, 121–125.

84. Okubo, T.S., Patella, P., D'Alessandro, I., and Wilson, R.I. (2020). A neural network for wind-guided compass navigation. Neuron *107*, 924–940.e18.

Please cite this article in press as: Barth-Maron et al., Interactions between specialized gain control mechanisms in olfactory processing, Current Biology (2023), https://doi.org/10.1016/j.cub.2023.10.041

STAR★METHODS

KEY RESOURCES TABLE

REAGENT or RESOURCE	SOURCE	IDENTIFIER
Experimental models: Organisms/strains		
D. melanogaster: *P{20XUAS-IVS-mCD8::GFP}attP40*	Barret Pfeiffer and Gerry Rubin	Pfeiffer et al.[74]
D. melanogaster: *P{GawB}NP1227*	Kyoto Drosophila Stock Center	RRID: DGGR_103945
D. melanogaster: *P{R67B06-Gal4}attP2*	Bloomington Drosophila Stock Center (BDSC)	RRID: BDSC_48294
D. melanogaster: *P{R70A09-Gal4}attP2*	BDSC	RRID: BDSC_47720, Pfeiffer et al.[75] and Jenett et al.[76]
D. melanogaster: *P{R24C12-Gal4}attP2*	BDSC	RRID: BDSC_49076, Pfeiffer et al.[75] and Jenett et al.[76]
D. melanogaster: *P{R78F09-Gal4}attP2*	BDSC	RRID: BDSC_40006, Pfeiffer et al.[75] and Jenett et al.[76]
D. melanogaster: *P{R26A01-lexA}attP40*	BDSC	RRID: BDSC_54113, Pfeiffer et al.[75] and Jenett et al.[76]
D. melanogaster: *PBac{20XUAS-IVS-jGCaMP7f}VK00005*	BDSC	RRID: BDSC_79031, Dana et al.[77]
D. melanogaster: *P{20XUAS-IVS-CsChrimson.mVenus}attP40*	BDSC	RRID: BDSC_55135, Klapoetke et al.[37]
D. melanogaster: *P{UAS-7xHalo7::CAAX}attP40*	BDSC	RRID: BDSC_67621, Sutcliffe et al.[78]
D. melanogaster: *P{13XLexAop2-mCD8::GFP}attP2*	BDSC	RRID: BDSC_32203, Pfeiffer et al.[74]
D. melanogaster: *P{UAS-GtACR1.d.EYFP}attP40*	BDSC	RRID: BDSC_92988, Mohammad et al.[38]
D. melanogaster: MCFO-3	BDSC	RRID:BDSC_64087, Nern et al.[28]
D. melanogaster: MCFO-4	BDSC	RRID:BDSC_64088, Nern et al.[28]
D. melanogaster: MCFO-5	BDSC	RRID:BDSC_64089, Nern et al.[28]
Deposited data		
Drosophila hemibrain v.1.2.1	https://neuprint.janelia.org	Scheffer et al.[20]
Software and algorithms		
MATLAB 2018a and 2021b	MathWorks	RRID: SCR_001622
ScanImage	Vidrio Technologies	RRID: SCR_014307, Pologrut et al.[79]
NoRMCorre	https://github.com/flatironinstitute/NoRMCorre	Pnevmatikakis and Giovannucci[80]
R 4.1.3	https://www.r-project.org/	RRID: SCR_001905
RStudio 2022.02.0	https://www.r-project.org/	RRID: SCR_000432
Python 3.7 and 3.9	https://www.python.org/	RRID: SCR_008394
Neuprint	https://neuprint.janelia.org/	Scheffer et al.[20]
neuprint-python	https://github.com/connectome-neuprint/neuprint-python	Berg and Schlegel[81]
NAVis	https://github.com/navis-org/navis	https://doi.org/10.5281/zenodo.4751181
model code	https://zenodo.org/	https://doi.org/10.5281/zenodo.10028674

RESOURCE AVAILABILITY

Lead contact

Further information and requests for resources and reagents should be directed to and will be fulfilled by the lead contact, Rachel Wilson (rachel_wilson@hms.harvard.edu).

Materials availability

This study did not generate new unique reagents.

Data and code availability

- All data reported in this paper will be shared by the lead contact upon request.
- Original code underlying computational models and necessary input data have been deposited at zenodo and are publicly available as of the date of publication. DOIs are listed in the key resources table.
- Any additional information required to reanalyze the data reported in this paper is available from the lead contact upon request.

EXPERIMENTAL MODEL AND STUDY PARTICIPANT DETAILS

Fly husbandry and genotypes

Flies used for electrophysiology and imaging experiments were females, because connectome data was only available for the female brain, and we wanted to ensure that our physiological data were relevant to female connectome data. Flies were reared in vials on Nutri-Fly GF German Food (Genesee Scientific #: 66-115) at 25°C and ~50-70% humidity on a 12 hour light-dark cycle, collected for experiments 16-72 hours post-eclosion. For optogenetics experiments flies were raised on a German food supplemented with 0.6 mM all-trans-retinal (Sigma #R2500), and fly vials were covered with foil to protect all-trans-retinal from photodegredation and to minimize unintended photostimulation. Flies were maintained in groups in their home vials (rather than isolated), and they were not exposed to previous experimental procedures prior to the experiments reported here. Genotypes of fly stocks used in each figure are as follows:

Figure 2:

LN2P:

w; P{20XUAS-IVS-mCD8::GFP}attP40 / +; P{R67B06-Gal4}attP2 / +*
P{R57C10-FLPL}su(Hw)attP8 / w; +; PBac{10xUAS(FRT.stop)myr::smGdP-HA}VK00005 P{10xUAS(FRT.stop)myr::smGdP-V5-THS-10xUAS(FRT.stop)myr::smGdP-FLAG}su(Hw)attP1 / P{R67B06-Gal4}attP2*
w / w+; +/+; P{R67B06-Gal4}attP2 / PBac{20XUAS-IVS-jGCaMP7f}VK00005*

LN2F_b:

w; P{20XUAS-IVS-mCD8::GFP}attP40 / +; P{R78F09-Gal4}attP2 / +*
P{R57C10-FLPG5.PEST}su(Hw)attP8 / w; +; PBac{10xUAS(FRT.stop)myr::smGdP-HA}VK00005 P{10xUAS(FRT.stop)myr::smGdP-V5-THS-10xUAS(FRT.stop)myr::smGdP-FLAG}su(Hw)attP1 / P{R78F09-Gal4}attP2*
w / +; +/+; P{R78F09-Gal4}attP2 / PBac{20XUAS-IVS-jGCaMP7f}VK00005*

LN1:

y w* / w*; P{GawB}NP1227 / P{UAS-7xHalo7::CAAX}attP40; +*
P{R57C10-FLPG5}su(Hw)attP8 / w; +; PBac{10xUAS(FRT.stop)myr::smGdP-HA}VK00005 P{10xUAS(FRT.stop)myr::smGdP-V5-THS-10xUAS(FRT.stop)myr::smGdP-FLAG}su(Hw)attP1 / P{R70A09-Gal4}attP2*
w / w+; +/+; P{R70A09-Gal4}attP2 / PBac{20XUAS-IVS-jGCaMP7f}VK00005*

LN2S/R:

w; P{20XUAS-IVS-mCD8::GFP}attP40 / +; P{R24C12-Gal4}attP2 / +*
P{R57C10-FLPG5.PEST}su(Hw)attP8 / w; +; PBac{10xUAS(FRT.stop)myr::smGdP-HA}VK00005 P{10xUAS(FRT.stop)myr::smGdP-V5-THS-10xUAS(FRT.stop)myr::smGdP-FLAG}su(Hw)attP1 / P{R24C12-Gal4}attP2*
w / w+; +/+; P{R24C12-Gal4}attP2 / PBac{20XUAS-IVS-jGCaMP7f}VK00005*

Figure 3:

LN2F_b:

w; P{20XUAS-IVS-mCD8::GFP}attP40 / +; P{R78F09-Gal4}attP2 / +*
w / +; +/+; P{R78F09-Gal4}attP2 / PBac{20XUAS-IVS-jGCaMP7f}VK00005*

LN2P:

w; P{20XUAS-IVS-mCD8::GFP}attP40 / +; P{R67B06-Gal4}attP2 / +*
w / w+; +/+; P{R67B06-Gal4}attP2 / PBac{20XUAS-IVS-jGCaMP7f}VK00005*

Figure 5:

LN2F_b:

w; P{R26A01-lexA}attP40 / P{20XUAS-IVS-CsChrimson.mVenus}attP40; P{13XLexAop2-mCD8::GFP}attP2 / P{R78F09-Gal4}attP2*

LN2P:

w; P{R26A01-lexA}attP40 / P{20XUAS-IVS-CsChrimson.mVenus}attP40; P{13XLexAop2-mCD8::GFP}attP2 / P{R67B06-Gal4}attP2*

Figure 6:

w; P{R26A01-lexA}attP40 / P{UAS-GtACR1.d.EYFP}attP40; P{13XLexAop2-mCD8::GFP}attP2 / P{R78F09-Gal4}attP2*

Figure S1:

P{R57C10-FLPL}su(Hw)attP8 / w; +; PBac{10xUAS(FRT.stop)myr::smGdP-HA}VK00005 P{10xUAS(FRT.stop)myr::smGdP-V5-THS-10xUAS(FRT.stop)myr::smGdP-FLAG}su(Hw)attP1 / P{R67B06-Gal4}attP2*

Please cite this article in press as: Barth-Maron et al., Interactions between specialized gain control mechanisms in olfactory processing, Current Biology (2023), https://doi.org/10.1016/j.cub.2023.10.041

Figure S2:
LN2P:
w; P{20XUAS-IVS-mCD8::GFP}attP40 / +; P{R67B06-Gal4}attP2 / +*
w / w+; +/+; P{R67B06-Gal4}attP2 / PBac{20XUAS-IVS-jGCaMP7f}VK00005*
LN2F_b:
w; P{20XUAS-IVS-mCD8::GFP}attP40 / +; P{R78F09-Gal4}attP2 / +*
w / +; +/+; P{R78F09-Gal4}attP2 / PBac{20XUAS-IVS-jGCaMP7f}VK00005*
LN1:
y w* / w*; P{GawB}NP1227 / P{UAS-7xHalo7::CAAX}attP40; +*
w / w+; +/+; P{R70A09-Gal4}attP2 / PBac{20XUAS-IVS-jGCaMP7f}VK00005*
LN2S/R:
w; P{20XUAS-IVS-mCD8::GFP}attP40 / +; P{R24C12-Gal4}attP2 / +*
w / w+; +/+; P{R24C12-Gal4}attP2 / PBac{20XUAS-IVS-jGCaMP7f}VK00005*
Figure S3:
LN2P:
w / w+; +/+; P{R67B06-Gal4}attP2 / PBac{20XUAS-IVS-jGCaMP7f}VK00005*
LN2F_b:
w / +; +/+; P{R78F09-Gal4}attP2 / PBac{20XUAS-IVS-jGCaMP7f}VK00005*
LN1:
w / w+; +/+; P{R70A09-Gal4}attP2 / PBac{20XUAS-IVS-jGCaMP7f}VK00005*
LN2S/R:
w / w+; +/+; P{R24C12-Gal4}attP2 / PBac{20XUAS-IVS-jGCaMP7f}VK00005*
Figure S4:
w; P{R26A01-lexA}attP40 / P{UAS-GtACR1.d.EYFP}attP40; P{13XLexAop2-mCD8::GFP}attP2 / P{R78F09-Gal4}attP2*
Figure S6:
w; P{R26A01-lexA}attP40; P{13XLexAop2-mCD8::GFP}attP2*

Origins of transgenic stocks

P{20XUAS-IVS-mCD8::GFP}attP40 was a gift from Barret Pfeiffer and Gerry Rubin.[74] *P{GawB}NP1227* was obtained from the Kyoto Drosophila Stock Center (103945). GMR Gal4 and GMR LexA lines[75,76] were obtained from the Bloomington Drosophila Resource Center (BDRC): *P{R67B06-Gal4}attP2* (48294), *P{R70A09-Gal4}attP2* (47720), *P{R24C12-Gal4}attP2* (49076), *P{R78F09-Gal4}attP2* (40006), *P{R26A01-lexA}attP40* (54113). The following UAS/LexAop transgenes were also obtained from the BDRC: *PBac{20XUAS-IVS-jGCaMP7f}VK00005* (79031), *P{20XUAS-IVS-CsChrimson.mVenus}attP40* (55135), *P{UAS-7xHalo7::CAAX}attP40* (67621), *P{13XLexAop2-mCD8::GFP}attP2* (32203), *P{UAS-GtACR1.d.EYFP}attP40* (92988), *P{R57C10-FLPL}su(Hw)attP8* (64087), *P{R57C10-FLPG5}su(Hw)attP8* (64088), *P{R57C10-FLPG5.PEST}su(Hw)attP8* (64089), *PBac{10xUAS(FRT.stop)myr::smGdP-HA}VK00005* (64087, 64088, 64089), *P{10xUAS(FRT.stop)myr::smGdP-V5-THS-10xUAS(FRT.stop)myr::smGdP-FLAG}su(Hw)attP1* (64087, 64088, 64089).

METHOD DETAILS

Experimental design

Our experimental designs did not involve any situations where animals were assigned to different treatment groups, and for this reason, randomization was not necessary. We used different genotypes as a means to express different fluorescent molecules in specific cell types (mCD8::GFP, GCaMP7f, CsChrimson.mVenus, GtACR1.d.EYFP); for this reason, the genotype of each fly was visually obvious to the experimenter, and blinding was not possible. Sample sizes were chosen in accordance with standard practices in the field, which are based on the expected level of fly-to-fly variability in each measurement type.

MultiColor FlpOut

MultiColor FlpOut (MCFO) was performed essentially as described previously.[28] Primary incubation solution contained mouse anti-Bruchpilot antibody (1:30, nc82, Developmental Studies Hybridoma Bank), rat anti-FLAG (1:200, Novus Biologicals #NBP1-06712B), rabbit anti-HA (1:300, Cell Signaling Technologies), and 5% normal goat serum (NGS) in PBST. Secondary incubation solution contained Alexa Fluor 488-conjugated goat anti-rabbit (1:250, Thermo Fisher Scientific #3724), ATTO-647-conjugated goat anti-rat (1:400, Rockland #612-156-120), and Alexa Fluor 405-conjugated goat anti-mouse (1:500, Thermo Fisher Scientific #3724) and 5% NGS in PBST. Tertiary incubation solution contained DyLight 550-conjugated mouse anti-V5 (1:500, MCA1360D550GA, Bio-Rad), and 5% normal mouse serum in PBST.

Odor delivery

An odor delivery tube (6mm ID PTFE, McMaster) was aimed at the fly at a fixed distance of 15 mm and angled at 22 degrees. A constant carrier stream of charcoal filtered medical-grade air flowed over the fly at a rate of 2 L/min. Odors were delivered into the carrier

Please cite this article in press as: Barth-Maron et al., Interactions between specialized gain control mechanisms in olfactory processing, Current Biology (2023), https://doi.org/10.1016/j.cub.2023.10.041

stream at a rate of 200mL/min using 3-port solenoid valves (Lee Co. LHDA1231415H), 10 mm before the end of the carrier tube. Whenever we added an odor stream to the carrier stream, we simultaneously removed a stream of non-odorized air with the same flow rate, in order to minimize changes in total air flow. Immediately prior to each experiment, each odor was mixed with 1 mL paraffin oil in a 2-mL screw-top vial at the specified dilution factor (vol/vol). Paraffin oil (J.T. Baker, VWR #JTS994) was stored under negative pressure for at least several days prior to use, in order to reduce the concentration of low-molecular-weight volatiles in the solvent. Odor vials were placed upstream of the solenoid valves, so that air could flow continuously through the odor vial headspace regardless of valve position; in this configuration odor concentration is a function of flow rate and partial pressure, rather than headspace saturation/depletion, which allows the delivery of prolonged odor pulses with minimal rundown in odor concentration. Since this results in odor contamination of the solenoid valve, a separate valve was swapped in for each concentration of each odor. Solenoid valves fed directly into the carrier stream, to minimize temporal smoothing of the odor concentration waveform. We verified odor waveform dynamics with a photoionization device (miniPID, Aurora Scientific; Figure S7), placed at the fly's location. Odor onset and offset had a time constant of ~20 ms, and no change in steady state odor concentration was detected on the timescale of seconds to minutes.

Stimuli

For imaging experiments, we used 2-s odor pulses, with an inter-pulse interval of 8 s. For electrophysiology experiments, we used trains of odor pulses at 0.28 Hz, 2.5 Hz, and 5 Hz. The 0.28 Hz stimulus consisted of 2-s pulses with 1.58-s inter-pulse intervals. The 2.5 Hz stimulus consisted of 20-ms pulses with 380-ms inter-pulse intervals. The 5 Hz stimulus consisted of 10-ms pulses with 190-ms inter-pulse intervals. These stimulus frequencies and duty cycles were chosen to natural odor stimuli, where odor encounters tend to be either brief and closely spaced, or else more prolonged and more widely spaced.[18] Between the end of one odor pulse train and the beginning of the next pulse train, we enforced a pause of at least 8 s. Pulse train stimuli were validated using a photoionization detector (PID, Figure S7), and these same pulse train stimuli were used as an input to our model.The exceptions were the model frequency tuning curves, where we used square waves (50% duty cycle) of frequency 0.03-11.22 Hz smoothed with a 30 ms exponential filter.

Fly preparation

Flies were cold anesthetized and secured in a hole in a horizontal platform consisting of.001" thick 302 stainless steel shim stock. A hole was photo-etched in this steel platform with a profile matching the fly's thorax and head (Etchit). This configuration allowed the dorsal part of the fly's head (and thorax) to be covered in saline, while the ventral head (including antennal segments a2 and a3), thorax, abdomen, and limbs remained dry. After saline was used to cover the dorsal part of the preparation, the antennal lobes were exposed by dissecting away a dorsal portion of the head capsule with fine forceps. Saline composition was 103 mM NaCl, 3mM KCl, 5 mM TES, 8 mM trehalose, 10 mM glucose, 26 mM $NaHCO_3$, 1 mM NaH2PO_4, 4mM $MgCl_2$, 1.5 mM $CaCl_2$, and was adjusted to have a pH of 7.1-3 and an osmolarity of 270-275 mOsm. Throughout each experiment, saline was bubbled with 95% O_2 / 5% CO_2 and it was perfused continuously over the preparation. The antennae were inspected immediately before the start of each experiment to ensure they remained dry and appeared healthy.

Electrophysiology

Whole-cell *in vivo* patch-clamp recordings were performed with an internal pipette solution composed of 140 mM KOH, 140 mM aspartic acid, 10 mM HEPES, 1 mM EGTA, 1 mM KCl, 4 mM MgATP, 0.5 mM Na_3GTP, and 13 mM biocytin hydrazide. Internal solution was adjusted to have a pH of 7.2 and an osmolarity of 265 mOsm. Patch pipettes (fabricated using a P-97 puller from Sutter Instruments) were made from borosilicate glass with O.D. 1.5 mm and I.D. 0.86 mm. Pipette resistance typically ranged from 6-10 MΩ. Cells were targeted for recording under an Olympus BX51 microscope with a 40x water-immersion objective. All recordings were performed in current-clamp mode with an Axopatch 200B amplifier and filtered with a 4-pole low-pass Bessel filter. Data was either filtered at 5 kHz and digitized at 10 kHz or filtered at 10 kHz and digitized at 20 kHz, using a National Instruments data acquisition board. Recorded voltages were corrected for a liquid junction potential of -13 mV.[82] Each cell was recorded in a different fly.

Optogenetics

To stimulate LNs using CsChrimson[37] we delivered blue light (490 nm) from an LED (ThorLabs M490L4) through the 40x water-immersion objective, with the light intensity attenuated by two neutral density filters in the light path (ND25 and ND3, Olympus). We further modulated light intensity with analog commands sent from the rig computer, set to modulate light intensity to 0%, 2.5%, 5%, 10%, 20%, 50%, or 100% of maximum power. This configuration resulted in power measurements at the sample of 0, 0.17, 0.48, 1.05, 2.40, 6.07, and 11.50 mW respectively. Light was timed so that it precisely coincided with the opening and closing of the valve that controlled odor delivery. To hyperpolarize LNs we used GtACR1[38,39] with the same light delivery configuration, but using only one light intensity (6.07 mW), which we confirmed was sufficient to block odor-evoked spiking in LN2F_b neurons. We did not test the effect of expressing GtACR1 in LN2P_c neurons because we were concerned about the possibility of GtACR1 expression in PNs in this genotype, given that in pilot experiments we observed that light hyperpolarized PNs and this effect persisted even after we pharmacologically blocked most network activity with 1 μM TTX. We did not see light-evoked PN depolarization when we depolarized LN2P_c cells with CsChrimson/light, suggesting that if this driver produces off-target Gal4 expression in PNs, this effect is genotype-dependent.

Please cite this article in press as: Barth-Maron et al., Interactions between specialized gain control mechanisms in olfactory processing, Current Biology (2023), https://doi.org/10.1016/j.cub.2023.10.041

Calcium imaging

In vivo calcium imaging was performed essentially as described previously,[83,84] with a two-photon laser scanning microscope (Bergamo II, Thorlabs) equipped with a resonant scanner (Vidrio). Two-photon excitation was achieved with a femtosecond Ti:Sapphire Laser with dispersion precompensation (Vision-S, Coherent) tuned to 940 nm. Imaging was done using a 20x objective (N.A. 1.0; XLUMPLFLN, Olympus) mounted on a fast piezoelectric objective scanner (P-725, Physik Instrumente). Emission fluorescence was filtered with a 525-nm bandpass filter (Thorlabs) and collected using a GaAsP photomultiplier tube (Hamamatsu). The imaging region was centered on the right antennal lobe. The imaging volume was 128×128 pixels and 15 slices deep in the z-axis (5 μm per slice), resulting in a ~6.5 Hz volumetric scanning rate. The volume encompassed almost the entire antennal lobe, except for a small ventral portion.

In vivo neuropil staining

At the end of each imaging experiment, we added 10 mL α-bungarotoxin-AlexaFluor488 solution (116 mM in saline) to the reservoir of saline around the brain, and we gently disrupted the glial sheath with fine forceps to increase permeability. The prep was then incubated with this solution for 20 minutes, followed by three saline washes of 2-3 min each. We then collected an image of the antennal lobe with the two-photon laser scanning microscope. This image was subsequently used to identify glomerulus boundaries and draw the borders of ROIs.

QUANTIFICATION AND STATISTICAL ANALYSIS

Connectomics analysis

To investigate the connectivity and morphology of Broad and Patchy cells, we analyzed a partial connectome of the dorsal part of the right central brain of an adult female fly obtained by the FlyEM Project at Janelia Research Campus[3] (https://www.janelia.org/projectteam/flyem/hemibrain). To conduct the analyses we used neuprint-python[81] (https://github.com/connectome-neuprint/neuprint-python) in conjunction with neuprint and the hemibrain v1.2.1 dataset (https://neuprint.janelia.org/). We began with a list of all 196 LNs innervating the right antennal lobe[3] (Table S1), and identified all synaptic partners with five or more synapses, in order to eliminate spurious connections. We ensured that this list contained the 2,644 identified ORNs and 338 identified PNs, and used it to generate an antennal lobe connectivity matrix. For Figure 3C we discarded all inputs that were not LNs, PNs, or ORNs, then summed and normalized inputs within each of our four LN subtypes of interest. For Figure 4A we kept all inputs and outputs, but placed connections that were not part of our six groups of interest into a 'miscellaneous' category. Example cells shown in Figure 2A are hemibrain IDs 1640909284 (LN2F_b), 2105086391 (LN2P_c), 1640887603 (LN1), 1732995501 (LN2S). Example cell shown in Figure 3A is hemibrain ID 1639886198. For Figure S3 we used NAVis (https://github.com/navis-org/navis) for morphological analyses. We retrieved meshes, and created skeletons with the MeshNeuron class' default 'wavefront' method (a wrapper for Skeletor). We then transformed the skeletons into the JRC2018F template brain space prior to doing morphometric analyses.

Electrophysiology data analysis

All analyses were done in MATLAB using custom code. Spikes were detected as local maxima using MATLAB's *findpeaks* function, and visually confirmed. Firing rates were calculated as kernel density estimates with a 150-ms hanning window centered at zero lag. Rate estimates were then downsampled to 1 kHz before further analysis. To analyze subthresold voltages, spikes were removed using a 40-ms median filter, then downsampled to 1 kHz before further analysis. To calculate the odor response peak-to-steady ratio, we divided the maximum rate within the first 350 ms by the maximum rate of the last 250 ms, here focusing on the 2-s stimulus. To generate frequency tuning curves, we projected the baseline-subtracted firing rate onto a version of the stimulus waveform that was normalized so the integral equaled 1, then centered; these frequency responses were then normalized so that the minimum trial-averaged response within each experiment was set to 0 and the maximum was set to 1.

Calcium imaging data analysis

Rigid motion correction was performed in the *x*, *y*, and z axes using NoRMCorre.[80] ROIs for glomerulus DC3 and the entire antennal lobe spanned multiple planes, and were initially drawn based on α-bungarotoxin staining of neuropil boundaries. ROIs were then adjusted slightly to account for imprecision in realignment, post-staining, and drift between trials that were not co-registered. For each trial a ΔF/F metric was calculated, with baseline fluorescence (F) defined as the mean fluorescence within ROI over a 1-s window immediately preceding odor onset. To calculate ΔF/F mean and standard deviation, individual traces were resampled at 1kHz to control for phase shifts between volume sample times and odor presentation. To quantify the degree to which 2-heptanone modulated DC3 farnesol responses, we computed ΔF/F (over the 2-s odor presentation period) and we normalized the response to the blend (farnesol + 2-heptanone) by the sum of the two individual component odor responses. Here a value of 1 implies linear summation, whereas a value <1 implies sublinear summation, and a value >1 implies supra-linear summation.

Statistical analysis

ANOVA and ANCOVA models were fit in MATLAB using the *anovan* function. Tukey post-hoc tests were performed in MATLAB using the *multcompare* function. Linear mixed-effects models were fit using the *formula* API of the python *statsmodels* package. Two-sample t-test was performed in MATLAB using the *ttest2* function. For Figure 3E we used a 2-way ANOVA with factors for cell type and spatial zone. For Figure 3F we used a linear mixed-effects model with a fixed effect for odor (blend vs farnesol) and a random intercept

Please cite this article in press as: Barth-Maron et al., Interactions between specialized gain control mechanisms in olfactory processing, Current Biology (2023), https://doi.org/10.1016/j.cub.2023.10.041

for between-cell effects. For Figure 3G we used a two-sample t-test. For Figures 5D and 5H we used 2-way ANCOVA models, with a categorical factor for stimulus frequency and continuous covariate for light intensity. For Figure 6C we used a mixed-effects ANOVA with two fixed-effects factors for light (on/off) and stimulus frequency, and a random factor for between-cell effects. For Figures 7C and 7D we used a mixed-effects ANOVA with two fixed-effects factors for 2-heptanone (present/absent) and stimulus frequency, and a random factor for between-cell effects.

Dynamical model

Figures 4 and 5 use a dynamical model that describes how neural activity varies over time, given some fluctuating odor concentration waveform. For simplicity, this model focuses on one glomerulus, and each cell type is represented by just one network node. The input to the model was a time-varying ORN firing rate ($s(t)$, with units of spikes/s). To model the ORN firing rate, we took the time-varying odor concentration profile (measured as the output voltage of a photoionization detector; see 'Odor delivery' above, Figure S7); we then scaled this waveform (by a factor a, with units of spikes/s), added a baseline offset value (b in units of spikes/s) representing spontaneous ORN activity,[6] and convolved it with a 30 ms exponential kernel to approximate the dynamics of olfactory transduction.[7] ORN neurotransmitter release ($u(t)$, with units of s^{-1}) varied as a function of ORN firing rate:

$$u(t) = (s(t) \cdot a + b) \cdot A(t) \cdot p(t) \quad \text{(Equation 1)}$$

where $A(t)$ is the fraction of available synaptic resources (e.g., available synaptic vesicles or neurotransmitter receptors) and $p(t)$ is the presynaptic vesicle release probability (with units of probability per spike, or $spikes^{-1}$). Both A and p are bounded at 0 and 1. As ORN release fluctuates, A is depleted and replenished:

$$\frac{dA}{dt} = -u(t) + \frac{(1 - A(t))}{\tau_a} \quad \text{(Equation 2)}$$

where τ_a is the time constant of synaptic resource replenishment (with units of s). Meanwhile, ORN neurotransmitter release excites a PN unit and an LN_pre unit. The LN_pre unit is recurrently connected with the ORN. Meanwhile, the LN_post unit is recurrently connected with the PN. PN and LN responses are given by the vector $r(t)$:

$$\tau_r \frac{dr}{dt} = -r(t) + ReLU(W \cdot u(t) + M \cdot r(t)) \quad \text{(Equation 3)}$$

where τ_r is the time constant of network activity (15 ms), W is the matrix of feedforward ORN→PN and ORN→LN_pre connections, M is the matrix of recurrent connections between the PN unit and the LN_post unit, and $ReLU$ denotes a rectifying-linear activation function. LN_pre drives presynaptic inhibition $I(t)$, which scales release probability $p(t)$:

$$p(t) = \frac{p_{rest}}{1 + I(t)}, \; I(t) = \sum_i r_i(t) \cdot \theta_{LN\_pre \rightarrow ORN} \quad \text{(Equation 4)}$$

where p_{rest} is the resting release probability (with no presynaptic inhibition), and $\theta_{LN\_pre \rightarrow ORN}$ gives the input weights from LN_pre onto the ORN.

To reduce complexity, we set all excitatory weights ($w_{ORN \rightarrow PN}$, $w_{ORN \rightarrow LN\_pre}$, $m_{PN \rightarrow LN\_post}$) to 1. Additionally, we constrained $m_{LN\_post \rightarrow PN}$ (in the matrix M) to -0.20 in order to ensure a reasonable parameter value despite partial redundancy that exists between $m_{LN\_post \rightarrow PN}$ and a during model fitting but not experimentation. The model then had five free parameters which specified the scale and offset of ORN firing (a, b), time constant of replenishment (τ_a), resting release probability (p_{rest}), and inhibitory synaptic weights ($\theta_{LN\_pre \rightarrow ORN}$). We fit these parameters by maximizing the correspondence between model PN responses and the recorded dynamics of 35 DC3 PNs using MATLAB's *fitnlm* function. Fitted values were as follows: a=1004.90 spikes/s, b=30.60 spikes/s, τ_a =3.84 s, p_{rest}= 0.006063, $\theta_{LN\_pre \rightarrow ORN}$=0.103. R^2 for the model fit was 0.806 for the 5 Hz stimulus, 0.831 for the 2.5 Hz stimulus, and 0.910 for the 0.28 Hz stimulus (0.849 in aggregate).

For experiments in Figure 5 we mimicked optogenetic activation by adding a smoothed and delayed version of the stimulus to either LN_pre or LN_post. Frequency tuning experiments were done with smoothed and delayed square waves, and activity injections were constant. For experiments in Figure 6 we mimicked optogenetic silencing by reducing the value of $\theta_{LN\_pre \rightarrow ORN}$ to 0.2 (~20% of fit value). We obtained frequency tuning curves by projecting model PN output onto a version of the stimulus waveform that was normalized so the integral equaled 1.

The competitive interactions between gain control mechanisms appear in this model as follows:

i) Global presynaptic inhibition reduces short-term depression - LN^{pre} activity drives presynaptic inhibition, which reduces release probability (Equation 4). This reduces ORN neurotransmitter release (Equation 1), which reduces depletion of synaptic resources (Equation 2).
ii) Global presynaptic inhibition reduces local postsynaptic inhibition - LN^{pre} activity drives presynaptic inhibition, which reduces release probability (Equation 4). This reduces ORN neurotransmitter release (Equation 1), which reduces LN^{post} activity (included in the vector $r(t)$, Equation 3).
iii) Short-term depression reduces global presynaptic inhibition - Depletion of synaptic resources (Equation 2) reduces ORN neurotransmitter release (Equation 1), which reduces LN^{pre} activity (included in the vector $r(t)$, Equation 3).

Please cite this article in press as: Barth-Maron et al., Interactions between specialized gain control mechanisms in olfactory processing, Current Biology (2023), https://doi.org/10.1016/j.cub.2023.10.041

iv) Short-term depression reduces local postsynaptic inhibition - Depletion of synaptic resources (Equation 2) reduces ORN neurotransmitter release (Equation 1), which reduces LN^{post} activity (included in the vector $r(t)$, Equation 3).

Population activity model

Figure 7 models population activity, specifically focusing on the time-averaged firing rate of large PN ensembles. We began with a model used by previous studies[47,48] that describes the effect of short-term synaptic depression and presynaptic inhibition on the vector of PN firing rates (r_{PN}):

$$r_{PN} = R_{max}\left(\frac{r_{ORN}^{1.5}}{\sigma^{1.5}+r_{ORN}^{1.5}+ms_{ORN}^{1.5}}\right) \quad \text{(Equation 5)}$$

where R_{max} is the maximum PN firing rate (165 Hz), σ is the ORN firing rate for which the PN response is half-maximum in the absence of inhibition (12 Hz). We took these values from previous study that fitted them values to PN electrophysiological data.[47] The term ms_{ORN} represents the effect of global presynaptic inhibition on PN responses, where s_{ORN} is the sum of all ORN firing rates for a given odor, and $m = 0.05$ (taken from Luo et al.[48]). The term r_{ORN} represents a vector of ORN firing rates, one for each odor stimulus, taken from electrophysiological data in Hallem and Carlson[6] We supplemented this data set with 24 simulated private odors (one for each ORN type) because some ORN types did not have private odors in the published data set. Thus, the input to the model included 200 odors in total. For the model without presynaptic inhibition, we set m to zero.

Next, we modeled the effect of intra-glomerular postsynaptic inhibition using a single exponential function of the form:

$$r_{LN\_post} = ae^{(br_{PN})} \quad \text{(Equation 6)}$$

where $b = 0.05$ and $a = 0.0496$. We chose b by inspection, and we calculated a such that the dynamic range of r_{LN_post} is the same as the dynamic range of r_{PN} for this dataset. The form of this function was intended to approximately reproduce the supralinear response of LN2P_x cells to increasing odor concentration (Figures 2D and 2E). We used r_{LN_post} to update r_{PN} as follows:

$$r_{PN} \rightarrow r_{PN} - w_{post} \cdot r_{LN\_post} \quad \text{(Equation 7)}$$

where $w_{post} = 0.2$. To assess odor discriminability we trained a set of 200 classifier neurons. Each classifier neuron was trained to respond selectively to one odor out of the full set of 200 (one-versus-rest classification). Weights were obtained by using Fisher's linear discriminant analysis (LDA) as described previously,[47,48] and a threshold was chosen to produce an approximately equal number of false positives and false negatives on our test set.[47,48] To generate training and test samples, we used a noise model described previously[48]:

$$r_{PN} \rightarrow r_{PN} + \delta \tanh(\alpha r_{PN})\eta \quad \text{(Equation 8)}$$

where $\delta = 10$ Hz, $\alpha = 0.025$ Hz, and η is a random variable with zero mean and unit variance. Training and test datasets were equal in size, with class-balanced positive and negative odors, such that each negative odor was repeated 10 times and each positive odor was repeated 200×10 times. Accuracies shown in Figure 7 were averaged over 100 initializations. Results for the no-inhibition model and the model with presynaptic inhibition are similar to those reported previously when LDA was used to obtain glomerular weights[48]; note that performance is qualitatively similar but quantitatively different when other methods are used.[48]

It should be noted that there are two forms of intra-glomerular gain control in this model: short-term synaptic depression, and intra-glomerular postsynaptic inhibition. These two forms of gain control have non-redundant effects on odor discrimination in our model. Short-term synaptic depression tends to produce saturation of the strongest odor responses, whereas intra-glomerular postsynaptic inhibition does not produce saturation.

The competitive interactions between gain control mechanisms appear in this model as follows:

i) Global presynaptic inhibition reduces short-term depression - In this static model, short-term depression is modeled as a saturating relationship between ORN firing rate and PN firing rate (Equation 5). Global presynaptic inhibition diminishes the tendency of PN firing rates to saturate as a function of ORN firing rates (Equation 5).
ii) Global presynaptic inhibition reduces local postsynaptic inhibition - Global presynaptic inhibition reduces PN activity (Equation 5), which reduces LN^{post} activity (Equation 6).
iii) Short-term depression reduces global presynaptic inhibition - This is included in the value of m, which is the parameter that specifies the magnitude of global presynaptic inhibition recruited by a given value of the summed ORN firing rate s_{ORN}. On average, the tendency of short-term depression to reduce global presynaptic inhibition will result in a lower value of m. In this model, we use a value of m that was previously fit to data, and so this phenomenon is simply captured in that fitted value.
iv) Short-term depression reduces local postsynaptic inhibition - Short-term depression causes PN firing rates to saturate as a function of ORN firing rates (Equation 5), and so reduces the recruitment of LN^{post} (Equation 6).